Solar Physics
DOI: 10.1007/•••••-•••-•••-••••-•

Solar Image Processing Techniques with Automated Feature Recognition (Invited Review)

Markus J. Aschwanden

Abstract We present a comprehensive and systematic overview of image processing techniques of solar data that use automated feature detection algorithms. We discuss the aspects of: (1) image pre-processing procedures; (2) automated detection of spatial features; (3) automated detection and tracking of temporal features (events); and (4) post-processing tasks, such as visualization of solar imagery, cataloguing, statistics, theoretical modeling, prediction and forecasting. For each aspect we highlight the most recent developments and science results. We conclude with an outlook on future trends.

Keywords: Data analysis techniques

1. Moore's Law and Science Return in Solar Physics

Why is there an increasing emphasis on automated image processing techniques in solar physics? Traditional observations in solar astronomy before 1960 included hand-drawings of sunspots on a projection screen behind a refractor telescope, occasional recordings of a solar spectrum, or an annual expedition to a tropical solar eclipse site. The gathered sunspot drawings were manually knitted into a solar cycle butterfly diagram, the solar spectrum recorded on a film was painstakingly measured under a microscope, and pictures from the 1919 solar eclipse led by Sir Arthur Stanley Eddington were visually measured with a ruler to prove Einstein's theory of relativity. These were all research projects that involved a managable amount of data that could be manually processed and led to significant scientific results without the necessity of automated data processing tools.

What changed dramatically the way of how we conduct research in any field after 1960 is the advent of computers. The escalating growth in manufacturing computer memories and the accelerated pace in building faster central processing units (CPUs) has been realized early on, expressed in what became to be known as *Moore's law* (e.g., Barrow 2008). Gordon Moore, co-founder of the computer

[1] Solar & Astrophysics Laboratory, Lockheed Martin
Advanced Technology Center, Bldg. 252, Org. ADBS, 3251
Hanover St., Palo Alto, CA 94304, USA email:
aschwanden@lmsal.com

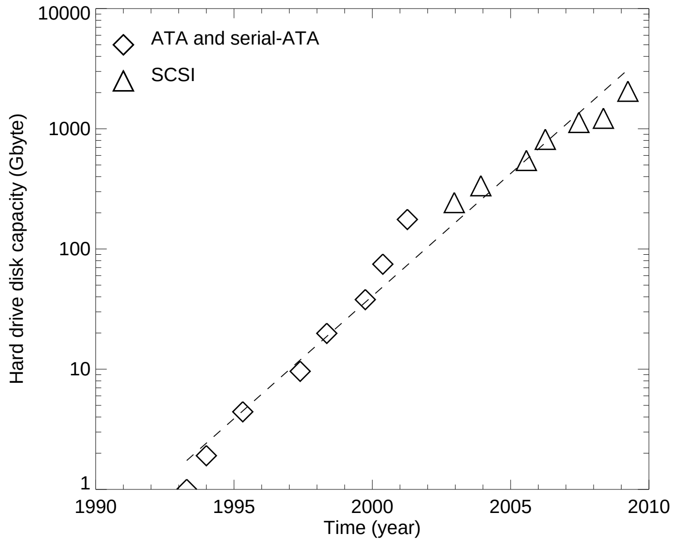

Figure 1. A modern version of Moore's law applied to the computer disk capacity (in Gigabytes) as a function of time (http://umbra.nascom.nasa.gov/images/Figure_1_200901.gif, courtesy of J.B. Gurman, for earlier versions see Gurman et al. 2002).

chip-manufacturing *Intel Corporation* and sponsor of the world's largest optical telescope (with 30 m mirrors), quantified the progress at the cutting edge of the computer chip industry by counting the number of transistors per die (i.e., on a rectangular waver of an integrated circuit) and found a nearly exponential growth as a function of time, published in the 19 April 1965 article of *Electronics Magazine*. It was the invention of the metal-oxide semiconductors (MOS) that enabled an astronomical growth of memory space and multiplied the microprocessor speeds, up to ten orders of magnitude over the last 50 years, in units of the original Moore's Law. Needless to say, that the increasing memory space led also to an avalanche-like growth of astronomical data gathered electronically with ground-based and space-based instruments, which clearly also requires adequate efficiency in data processing, and hence, the demand for automated image processing techniques. However, besides the obvious gain in efficiency and quantity of the data volume, a much more fundamental aspect of automated image processing is the objectivity, precision, and statistical significance we achieve in scientific analysis with automated numerical computer algorithms.

In order to illustrate Moore's law in terms of storage ressources of solar data, we can look at the disk capacity of hard drives as a function of time over the last two decades, which presently just exceeded 1 Terabyte (= 10^{12} bytes), as shown in Fig. 1. The soon to be launched *Solar Dynamics Observatory (SDO)* is expected to overwhelm us solar physicists with such a state-of-the-art downlink data rate of 1.5 Terabyte a day, which we clearly cannot handle without automated image processing tools. The data flow rate is staggering, multi-wavelength images will flood in with with a rate of 1 image (4k×4k) per second, compared

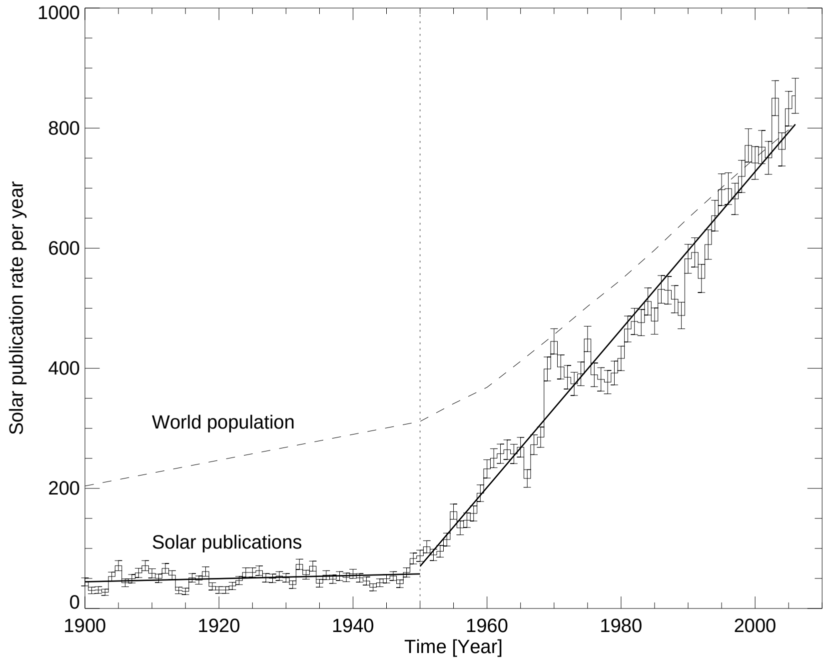

Figure 2. The rate of publications in solar physics over the last century, based on searches in NASA's ADS database. The histogram shows the annual publication rate, which is fitted with linear regression fits before and after 1950. For comparison, we show also the relative growth of the world population, normalized to the peak value at 2006, which grew from 1.65 billion humans in 1900 to 6.45 billions in 2006. Note the abrupt change in both evolutions after 1950.

with 1 image (2k×2k) every 3 minutes from STEREO, or 1 image every 12 minutes from SOHO.

Quantity, of course, is not everything, and many researchers justifyably argue that the science return may ultimately depend more on the quality of research. Is there any correlation between quantity and quality of research? In order to address this question we plot the rate of peer-reviewed publications in solar physics over the last century, as shown in Fig. 2. We constructed this histogram from annual searches of solar papers in NASA's *Astrophysical Database System (ADS)* with well-chosen solar keywords and systematic corrections for ambiguous selections (such as filtering out papers on "extra-solar planets" or "solar-like stars" that come up when searching for papers that contain the word "solar" in the title or abstract). The histogram shown in Fig. 2 contains an estimated number of $\approx 27,500$ (refereed) solar publications during the time interval of 1900-2006. Interestingly, the publication rate was extremely constant before 1950, with a leasurely average of ≈ 50 papers per year, while it suddenly started to grow afterward with an average increase of ≈ 13 papers per year, a trend that already lasts for six decades. Note also a remarkable spike after 1967, when the journal *Solar Physics* was founded.

The relative growth rate of the world population shows a similar evolution with a significantly faster growth rate after 1950, but both exhibit linear rather than exponential growth. Technological and economical conditions definitely improved to such a degree after 1950 that productivity in science rapidly accelerated. An additional factor is the release of a large number of scientists and engineers previously employed in the second world war effort. If we compare the progress in computer technology according to Moore's law shown in Fig. 1, we note that data storage and processing capacity grew exponentially after 1960, while science results measured in terms of publications grew linearly after 1950 (Fig. 2), so we may conclude that science return scales approximately logarithmically with the amount of available data. This is an important lesson that underscores the need for automated data processing methods in order to keep up with current growth in science return. In other words, without the development and availability of automated data processing tools we could not digest the exponentially increasing amount of data and predictably would fall back in our science productivity.

2. Image Pre-Processing Procedures

After this prelude of Moore's law we turn now to processing of solar data. Every successful automated feature detection algorithm requires a number of image pre-processing steps, which mostly serve the purpose to suppress the wrong (instrumental, nonsolar, non-selected) features, spurious signals, or inaccurate measurements. In Table 1 we list a number of image processing categories with examples of effects and required correction steps that need to be applied to solar images. It is beyond the scope of this review to describe all the technicalities of these image pre-processing steps in excruciating detail, but we rather want to exemplify a few typical applications and point out some interesting consequences that these effects have on automated feature detection algorithms.

2.1. Instrumental effects

For charge-coupled devices (CCDs) as they are used in all space-borne telescopes operating in soft X-ray (SXR) and extreme ultraviolet (EUV) wavelengths, such as the Yohkoh, SOHO, TRACE, STEREO, Hinode, or the SDO mission, the pixelized images are not always perfectly even, but contain up to $\lesssim 0.1\%$ "bad" pixels (e.g., Aschwanden et al. 2000a), which show either a permanent under-efficiency (probably due to fabrication artifacts) and are called "dark pixels", or produce temporarily a too high readout current (probably because some electrons are not properly flushed out after CCD readout), which are called "hot pixels". Ignoring such artifacts would lead to false detections of small-scale phenomena, such as nanoflares (Krucker and Benz 1998; Parnell and Jupp 2000; Aschwanden et al. 2000b). Uneven sensitivity across the CCD area is usually compensated by subtracting a DC pedestal value or "dark current" image. Solar images are not always rectangular, although the CCD readout is, but may have "vignetting" in the image corners that are occulted by the aperture, or "silhouetting" in the central part of the image due to occulter disks (in coronagraphs)

Table 1. Image pre-processing procedures

Image processing category	effect or correction
instrumental effects	hot or dark CCD pixels (EUV)
	flatfielding, DC pedestal (EUV)
	vignetting (aperture, field-of-view)
	silhouetting (telescope spider)
	occulter disk (coronagraphs)
	data recording gaps
	telemetry gaps (spacecraft)
	image compression (jpeg, ICER)
	aberration (focusing optics)
	non-quadratic pixels (CCD pixel platscale)
nonsolar features	cosmic-ray spikes (EUV)
	interference lines (radio spectra)
image resolution	rebinning, resampling, bilinear interpolation
	unresolved structures, filling factor
	point-spread function deconvolution
	blind iterative deconvolution
image background	subtract quiet Sun emission (SXR, EUV)
	subtract center-limb profile (white light)
	straylight (optical, EUV)
	star field removal (STEREO/COR,HI)
coordinate system	heliographic coordinates (solar images)
	ecliptic coordinates (heliospheric images)
	epipolar coordinates (STEREO images)
image coalignment	cospatial wavelengths filters
	cospatial time sequence
	Sun-spacecraft distance (STEREO)
	spacecraft roll angle
	differential solar rotation
	spacecraft pointing/jitter
	multi-spacecraft observations (STEREO)
image filtering	photon Poisson noise
	Poisson recoding
	boxcar smoothing
	image stacking (time sequence)
	Fourier filter, optimum filter
	lowpass, highpass filtering
	wavelet denoising
	edge enhancing, unsharp masking
	Kalman filter
	morphological filter
image reconstruction	Fourier imaging (radio, hard X-rays)
	demodulation (spinning spacecraft)
	speckle image reconstruction (seeing)
	phase diversity (seeing)

or shadows from mechanical support structures (also called spiders) that hold a secondary mirror on the optical axis in place. Although the resulting shadows in the images are often obvious by visual inspection, ignoring their area correction can lead to incorrect flux or event rate normalizations in automated feature detection codes. The same is true for data recording gaps or telemetry gaps, which can render incomplete images with empty blocks or non-uniform time series (which are particularly annoying for Fourier and wavelet analysis). A rather subtle instrumental effect is image compression, which usually is close to loss-less compression, but can affect the Poisson noise statistics and introduce artificial features in low-count areas of images, which can be retrieved by Poisson recoding (Nicula et al. 2005). Instruments with focusing optics have to deal with image distortions such as aberration and astigmatism. Images from CCDs need a proper characterization of their pixel platscale, some CCDs may have rectangular pixels, especially slit-scan spectrograhs (e.g., SoHO/CDS or SUMER).

2.2. Nonsolar Features

Since our main goal is to design automated algorithms that detect and measure solar phenomena (i.e., features), we certainly want to suppress nonsolar features, such as cosmic rays, high-energy electron or proton hits (frequently occurring for spacecraft orbits crossing the VanAllen Belt or the Earth's magnetospheric cusps near the poles). Such nonsolar signals have often the characteristics of single-pixel high values that do not persist in subsequent images, but can also have the shape of streaks for small incidence angles, which can be removed from the images with "despiking" and "destreaking" algorithms, for instance by using a *mathematical morphology filter* (Marshall et al. 2006). Alternatively, one can "abuse" EUV cameras by counting such particle hits intentionally to monitor the particle flux after a huge Earth-directed coronal mass ejection (CME) (Sam Freeland, private communication).

Somewhat more down to Earth, a lot of disturbances that affect solar radio images or radio dynamic spectra are man-made, in particular from radio and TV stations operating at metric and microwave wavelengths, which challenge image reconstruction from radio interferometers (e.g., VLA, OVRO, Nançay, Nobeyama). New algorithms that detect data anomalies (e.g., nonsolar disturbances) are currently developed (Csillaghy 2009).

2.3. Image Resolution

Insufficient instrumental resolution can play many tricks to feature measurements, left alone to automated detection of features. A classical example is an unresolved loop thread, even when observed with the currently highest resolution in EUV (of $\approx 1''$ with TRACE; Fig.3 right). Unresolved loop width variations can lead to filling factors that vary from pixel to pixel, underestimated electron densities (inconsistent with spectrometers), incorrect hydrostatic scale heights, and a magnetic field divergence that is inconsistent with magnetic field extrapolations (DeForest 2007). Feature recognition using different wavelength filters or different instruments require rebinning or resampling to an identical

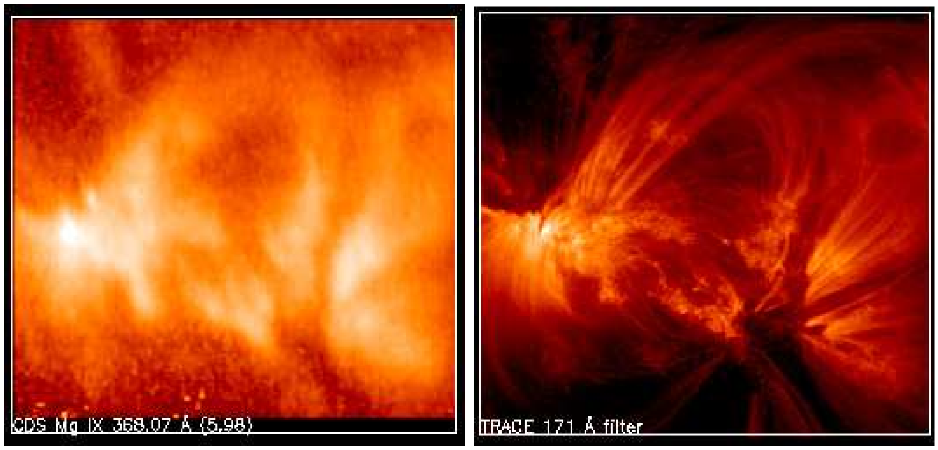

Figure 3. *Left:* A SoHO/CDS Mg IX, 368.07 Å (log(T)=5.98) image of a coronal loop bundle. *Right:* A simultaneous TRACE 171 Å (log(T)=6.0) image of the same loop structure. Note that the CDS loop structure consists of at least 10 loop threads that are resolved in the TRACE image.

spatial resolution, but the simplest algorithms such as bilinear interpolation may not preserve the Poisson statistics. Quadratic and fourth-order polynomial interpolation schemes that reproduce the pixelwise photon counts exactly were developed by Sakurai & Shin (2001). An optimized resampling algorithm that conserves the input sampling area in the output pixel requires coordinate transformation with padded ellipses (DeForest 2004). Ideally, the spatial resolution of the instrument is exactly characterized in terms of a point-spread function and images should first be deconvolved. The point spread function of an instrument can be determined from blind iterative deconvolution, either from single images (e.g., Yohkoh/SXT; Karovska and Hudson 1994; Gburek et al. 2002), or from multiple images with different degradations (multi-channel blind deconvolution; Simberova and Flusser 2005; Simberova et al. 2009).

2.4. Image Background

Feature definition almost always requires a threshold, which separates out feature -unrelated background. Since features display a large variety of morphological and geometric structures, the complementary background structure is equally multi-facetted and is often not trivial to define. For instance, how can a coronal loop structure be defined in the two images in Fig. 3? If we set a simple flux threshold, we find the bright "moss" structure or the denser footpoint segments of loops (due to their gravitational stratification), but miss the fainter loop tops. If we set the flux threshold very low so that the faint loop tops are included, we end up with contours that encompass entire active regions, rather than individual loops. Thus, a background subtraction by a simple threshold setting does generally not work for loop feature detection, and we have to resort to more sophisticated image enhancement and filtering techniques that are able to define more suitable image background models (see §2.7).

Besides the background of feature-unrelated structures, there is also an instrument-related background flux, such as straylight produced by diffraction through the telescope aperture, obscurations along the optical path, mirror imperfections, or reflection and scattering in the detector at the focal plane (e.g., DeForest et al. 2009), often characterized by an instrumental point-spread function. This background can be eliminated by a deconvolution of the image with the 2D point-spread function. The scattered light in TRACE images was found to amount up to 19% from an analysis of the diffraction patterns (Lin et al. 2001), while a deconvolution analysis of the Venus transit found up to 43% (DeForest et al. 2009).

The background definition always depends on the feature definition because of its complementarity. If you want to detect sun-grazing comets in STEREO/COR2 or HI images, you want to filter out the diffuse background white-light emission from the solar wind and coronal mass ejections, but if you are interested in coronal mass outflows, you want to remove the background star field (e.g., Davis et al. 2008).

2.5. Coordinate System

As soon as more than one solar image is involved in automated feature tracking, images have to be coaligned in identical coordinate systems. The information on the coordinate system used in an astronomical image has its long-standing heritage in the standards of FITS header descriptors (Grosbol et al. 1988, Harten et al. 1988, Wells et al. 1981), implemented in the *Solar Software (SSW)* (*http://www.lmsal.com/solarsoft*), and has been extended to multi-spacecraft data such as the STEREO mission (Thompson 2006). Most coordinate transformations of images can automatically be carried out with SSW routines, but solar imagery entertains a larger variety of coordinate systems than non-solar astronomical data. The original FITS coordinate system has been generalized to the *world coordinate system (WCS)* to allow for various map projections in spherical coordinates (Thompson 2006). Solar images are generally transformed into heliographic coordinates (in terms of solar latitudes and longitudes), either into Stonyhurst heliographic coordinates (with a fixed Earth-Sun axis) or into Carrington heliographic coordinates (which rotates with the mean solar rotation rate). Heliocentric coordinates quantify the 3D coordinates relative to the center of the Sun, such as the *Heliocentric Aries Ecliptic (HAE)*, the *Heliocentric Earth Ecliptic (HEE)*, or *Heliocentric Earth Equatorial (HEEQ)* system. For spacecraft observations at some distance from the Earth, such as from the two STEREO spacecraft, the WCS coordinate transformations have also to include the varying distances of the spacecraft from the Sun and the differing roll angles of the two spacecaft. For stereoscopic triangulation, a useful coordinate system is given by epipolar planes (Inhester 2006), referenced to the plane that intersects the two spacecraft positions and the Sun center.

Whenever a coordinate transformation of images is involved, the user has to be aware that the transformed image is subject to bilinear interpolation or resampling of some kind (DeForest 2004), which changes the photon statistics per pixel and may introduce more data noise. Proper consideration of this image modification is particularly important for automated detection algorithms that detect faint features above some user-selected noise threshold.

2.6. Image Coalignment

Ideally, image coalignment can blindly be carried out by SSW software that uses the FITS header information (see descriptions of SSW procedures in *http://www.lmsal.com/solarsoft*). This automated coalignment was often unsatisfactory earlier on, when the satellite pointing or pointing jitter was not known with subpixel accuracy, but is generally reliable to-date, in particular for full-Sun images where the limb automatically can be fitted to constrain the Sun center position. However, even with fine-pointing systems driven by guiding telescopes (similar to adaptive optics), small misalignments between the guiding telescope and the optical axis of the main telescope can occur due to temperature (bending) effects, e.g., when the TRACE spacecraft emerges out of the nightside part of its orbit into daylight, causing misalinments in the order of a few arcseconds (e.g., Aschwanden et al. 2000a).

Alternative coalignment procedures are based on cross-correlation of images, which works very well for static phenomena (such as the solar disk as a whole), but can reveal amazing displacements for dynamic phenomena (such as granulation, bright points, flares, CMEs). Even when averaged over a large field-of-view, erratic motions do not always cancel out, because the dynamics of the brightest features dominate the offsets found in cross-correlation coefficients. A possible strategy could be to mask out all bright dynamic features and to use only faint image segments.

Coalignments have to be performed for mutli-wavelength images for any kind of temperature and density diagnostics, but different temperature filters show often disparate, non-identical, non-cospatial features that should not be coaligned by means of cross-correlation. Coalignments have to be applied to automated feature tracking in time series of images (data cubes), where imperfect coalignment will lead to truncated time evolutions and underestimated durations and fluxes in single-pixel time series. Single-pixel time series can only be extracted if the solar (differential) rotation is compensated (i.e., in the Carrington coordinate system), which is particularly important for automated detection of time-variable phenomena. These are just a few of the manifold intricacies where poor image coalignment can spoil automated feature detection.

2.7. Image Filtering

Applying a filter to an image allows us to bring out or to enhance features of selected spatial scales, while feature-unrelated structures (i.e., background noise) are suppressed. Image filtering techniques are thus of utmost importance for automated feature detection algorithms. The most commonly used filters are noise filters that eliminate the photon Poisson noise (denoising), which can be done as simple as with a boxcar smoothing function (i.e., replacing each pixel value by the average of a surrounding area of selected size). Stacking of images reduces also the photon noise, because the signal-to-noise ratio improves with

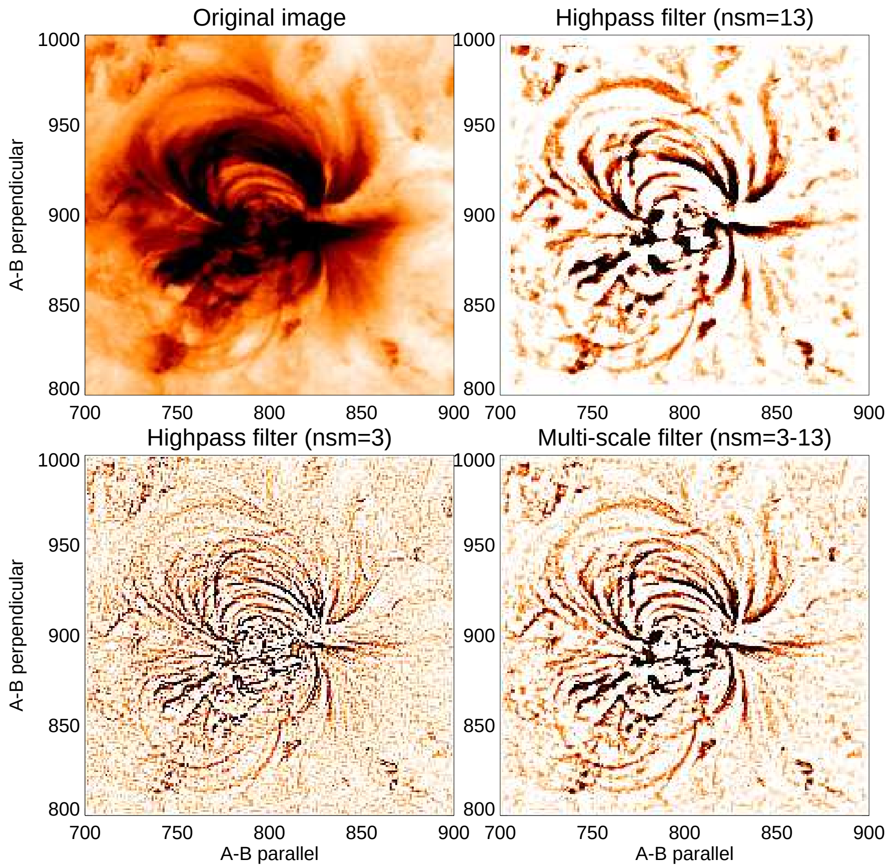

Figure 4. A part of a 171 Å image (pixel range x=700-900, y=800-1000) observed with STEREO/EUVI on 2007-May-09, 20:40:45 UT, is shown as original image with a linear color scale (top left), after highpass filtering with a boxcar of $n_{sm} = 3$ pixels (bottom left), with a boxcar of $n_{sm} = 13$ pixels (top right), and after multi-scale filtering with boxcars of $n_{sm} = 3, 5, ..., 13$ (bottom right). Note that the multi-scale filter enhances both finer and wider structures with a balanced weighting and allows a more reliable loop tracing [Aschwanden et al. 2009a].

the square root of the number of photons. Image filtering is often performed in the (spatial) frequency domain using the Fourier transform (i.e., Fourier filtering). A discrete Fourier power spectrum is computed from an image, which contains all the image information in terms of spatial scales and phases, which can then be back-transformed (with the inverse Fourier transform) to retrieve the original image. If one truncates the (complex) Fourier power spectrum at the low-frequency side before back transformation, we filter out the low frequencies (i.e., large spatial structures), which is called a high-pass filter (see examples in Fig. 4). Vice versa, if the high-frequency part is cut off before back transformation, we have a low-pass filter. Combining the two (low- and high-frequency) cutoffs, we have a bandpass filter that contains only features with a selected spatial scale range. A variant of the Fourier filter is the so-called *optimum filter*, where the frequency components in the Fourier spectrum are weighted in such a way that the exact signal (or feature) and a superimposed noise is assumed to be independent of the signal. Fine structures can be drastically enhanced by *unsharp masking*, which consists simply of subtracting a smoothed or lowpass-filtered image from the original image. These are all standard methods that are frequently used in the restoration of astronomical data.

Image filters for solar images have been designed as customized techniques that are idiosyncratic to solar features, such as sunspots, filaments, coronal loops, flares, or CMEs. An introduction into image standardization and enhancement is given in §2 by Ipson et al. in the monograph *Artificial intelligence in recognition and classification of astrophysical and medical images* (Zharkova and Jain 2007). Image enhancing methods using iterative maximum likelihood algorithms with sub-pixel sampling were developed for blurred images with a known point-spread function, e.g., for IRIS images (Roumeliotis 1995) or Yohkoh/SXT images (Sylwester and Sylwester 1998, 1999, 2004). Another novel (non-standard) image-processing technique based on multi-scale wavelet packet equalization enhances and visualizes the crispy finestructure in SOHO/EUV and STEREO/EUVI images quite efficiently (Stenborg and Cobelli 2003; Stenborg et al. 2008). However, we have always to bear in mind that these image enhancing filters are all of nonlinear nature. The enhanced images are very powerful for automated feature detection regarding morphology and geometry, but cannot be used for quantitative flux measurements (e.g., for temperature and density diagnostics).

2.8. Image Restoration and Reconstruction

Solar images recorded in optical wavelengths suffer from distortions caused by air turbulence in the Earth's atmosphere (i.e., the "seeing", characterized by the spatial scale of the coherence length, called Fried's parameter). There are two major techniques used to restore seeing-degraded solar images: the speckle interferometry and the phase diversity method. Speckle imaging uses a series of images with very short exposure times ($\lesssim 10$ ms), so that the turbulent motion of the atmosphere is too slow to have an effect and the speckles recorded in the image represent a snapshot of the atmospheric seeing. The short exposure images can then be coaligned to the brightest speckles and averaged together. The phase diversity method estimates the wavefront aberrations over isoplanatic areas from multiphase images, where the multiphase images have known phase differences (recorded in different focus positions), from which an improved image can be synthesized. Recent applications of speckle imaging include data from the Vacuum Tower Telescope (VTT) at Tenerife, which reveal the dynamic evolution of sunspot fine structures, umbral dots, penumbral grains close to the telescopic diffraction limit of $0.16''$(Denker 1998), near real-time reconstruction of images from Big Bear Solar Observatory (BBSO) (Denker et al. 2001; Yang et al. 2003), estimation of Fried's parameter from long-exposure solar images (Sridharan et al. 2002, 2004), high resolution solar speckle imaging with an extended Knox Thompson algorithm (Mikurda and Van der Luehe 2006; Mikurda et al. 2006), or differential speckle interferometry of the photosphere (Grec et al. 2007). Speckle imaging is also used for non-solar data, for instance in the search of exoplanets (Soummer et al. 2007). Recent applications of the phase diversity method include the first implementation of phase diversity at THEMIS (Criscuoli et al. 2005), phase diversity restoration of sunspot images from the Swedish Vacuum Solar Telescope at La Palma (Bonet et al. 2004), or solar image restorations by use of multi-frame blind deconvolution with multiple objects and phase diversity (Van Noort et al. 2005).

Solar images in radio wavelengths or hard X-rays are generally reconstructed with Fourier-type imaging, although for different reasons. Radio wavelengths are very long and thus direct imaging with high angular resolution can only be achieved at the shortest (millimeter and centimeter) wavelengths with very large radio dishes, while the longer wavelengths (decimetric, metric) require interferometers. Introductions into radio interferometry and Fourier synthesis imaging can be found in Perley et al. (1980) and Bastian (2006). A spatial and spectral maximum entropy method applied to Owens Valley Radio Observatory data is described in Komm et al. (1995).

X-rays, in contrast, have very short wavelengths that can only be focused by total reflection at very small angles, which are the smaller the higher the energy of the hard X-ray photons. Hard X-ray imaging, therefore, is accomplished by collimators made of grids at various spatial scales that transmit and absorb hard X-rays based on their angle of incidence and interference. The Ramaty High Energy Solar Spectroscopic Imager (RHESSI), for instance, is of the class of rotation-modulated collimators that spins and samples Fourier components of 9 different spatial scales at all roll angles during a rotation period of 4 s. This provides a large number of Fourier components that have to be synthesized into a spatial image. RHESSI imaging can be performed with at least 7 different image reconstruction algorithms, such as *Clean, Maximum Entropy Method (MEM), Maximum Entropy Visibilities (MEMVis), Pixon*, and *Forward-Fitting* (Hurford and Curtis 2002; Hurford et al. 2002; Metcalf et al. 1996a,b; Puetter 1995, 1996; 1997; Puetter and Yahil 1999; Aschwanden et al. 2002, 2004).

3. Automated Detection of Spatial Features

After all the pre-processing we are now ready to proceed to automated feature recognition techniques, which includes detection, identification, and classification of features. In this section we restrict ourselves to *spatial features* (without time dependence), while the extension into the time domain, i.e. the automated tracking of *spatio-temporal features* is treated in the next section 4. In this section we subdivide different methods according to their complexity, starting with one-dimensional (1D) curvi-linear features (§3.1), two-dimensional (2D) region or area features (§3.2), spectral (wavelet or multi-scale) feature analysis (§3.3), and more complex algorithms that employ a feedback mechanism, techniques that are also called *neural learning* or *artificial intelligence*. A list of algorithms and their applications to solar features with references is given in Table 2.

Table 2. Automated Detection Algorithms applied to Solar Spatial Features: L=Loop, S=sunspots, M=magnetic field, A=active regions, F=filaments, P=prominences, H=coronal holes, X=soft X-ray sigmoids, G=Granulation.

Feature Detection Algorithm	L	S	M	A	F	P	H	X	G
Curvi-linear 1D feature recognition									
(1) Oriented-connectivity method	L								
(2) Dynamic aperture-based loop segmentation	L								
(3) Unbiased detection of curvilinear structures	L								
(4) Oriented-directivity loop tracing	L								
(5) Ridge detection by automated scaling	L								
(6) Ellipse detection, inverse Hough transform	L								
Region-based 2D feature recognition									
(7) Contrast (threshold) and contiguity		S		A					
(8) Region-based feature recognition		S							
(9) Mathematical morphology		S							
(10) Euclidian distance transform, labelling			M						
(11) Region growing, boundary extraction				A					
(12) Smoothing, thresholding, centroiding				A					
(13) Thresholding, morphological closing					F				
(14) Region growing, skeleton pruning					F				
(15) Thresholding, morphological filtering					F			X	
(16) Histogram segmentation, thresholding						P			
(17) Histogram-based intensity thresholding							H		
(18) Region-growing, histogram-based segmentation					F		H		
Spectral Methods of Feature Detection									
(19) Daubechies wavelet transform				A					
(20) Hurst's rescaled range analysis				A					
(21) Fractal analysis (box counting, Jaenisch)				A					
(22) Wavelet analysis (*á trous algorithm*)	A				F				
(23) Singular spectrum analysis		S			F				
(24) Multifractal analysis				A					
(25) Gradient pattern, discrete wavelet decomposition					F				
(26) Multi-scale Laplacian-of-Gaussian operator									G
(27) Fractal-based fuzzy segmentation				A					
Neural Network Learning (NNT) Algorithms									
(28) Artificial neural nework, back-propagation					F				
(29) Labelling, unsupervised clustering		S							
(30) Autoassociative artificial neural network		S							
(31) Intensity thresholding, neural network		S							
(32) Supervised segmentation, Bayesian classifier				A			H		
(33) RIPPER, multi-layer perceptron, Adaboost	L								
(34) Thresholding, Neural network learning		S							
(35) Supervised segmentation, Bayesian classifier							H		
(36) Support Vector Machines						P			

References: 1 (L): Lee et al. (2004, 2006a); 2 (L): Lee et al. (2006b); 3 (L): Smith (2005); 4 (L): Aschwanden et al. (2008a); 5 (L): Inhester et al. (2008); 6 (L): Sellah and Naraoui (2008); 7 (S,A): Preminger et al. (2001), Jones et al. (2008); 8 (S): Zharkova and Jain (2007); 9 (S): Zharkov et al. (2005a,b), Zharkov and Zharkova (2006), Zharkova et al. (2003); Benkhalil et al. (2006), Curto et al. (2008); 10 (M): Ipson et al. (2005, 2009); 11 (A): McAteer et al. (2005); 12 (A): LaBonte et al. (2007), Georgoulis et al. (2008); 13 (F): Shih and Kowalski (2003); 14 (F): Fuller et al. (2005); 15 (F): Bernasconi et al. (2005), Bernasconi and Georgoulis (2009); 16 (P): Foullon and Verwichte (2006); 17 (H): Krista and Gallagher (2009); 18 (F,H): Scholl and Habbal (2008), 19 (A): Komm (1994, 1995); 20 (A): Adams et al. (1997); 21 (A): Stark et al. (1997); 22 (A,F): Portier-Fozzani et al. (2001); 23 (S,F): Lefebvre and Rozelot (2004); 24 (A): Abramenko (2005), Georgoulis (2005, 2009), Conlon et al. (2008), Hewett et al. (2008), Ireland et al. (2008); 25 (F): Rosa et al. (2008); 26 (G): Berrilli et al. (2005); 27 (A): Revathy et al. (2005); 28 (F): Zharkova and Schetinin (2005); 29 (S): Turmon et al. (2002); 30 (S): Socas-Navarro (2005a,b); 31 (A): De Wit (2006), De Wit et al. (2009), 32 (S,H): Colak and Qahwaji (2008); 33 (L): Durak et al. (2009); Durak and Nasraoui (2009); 34 (S): Colak and Qahwaji (2008), 35 (H): De Wit (2006), De Wit et al. (2009); 36 (P): Labrosse et al. (2009);

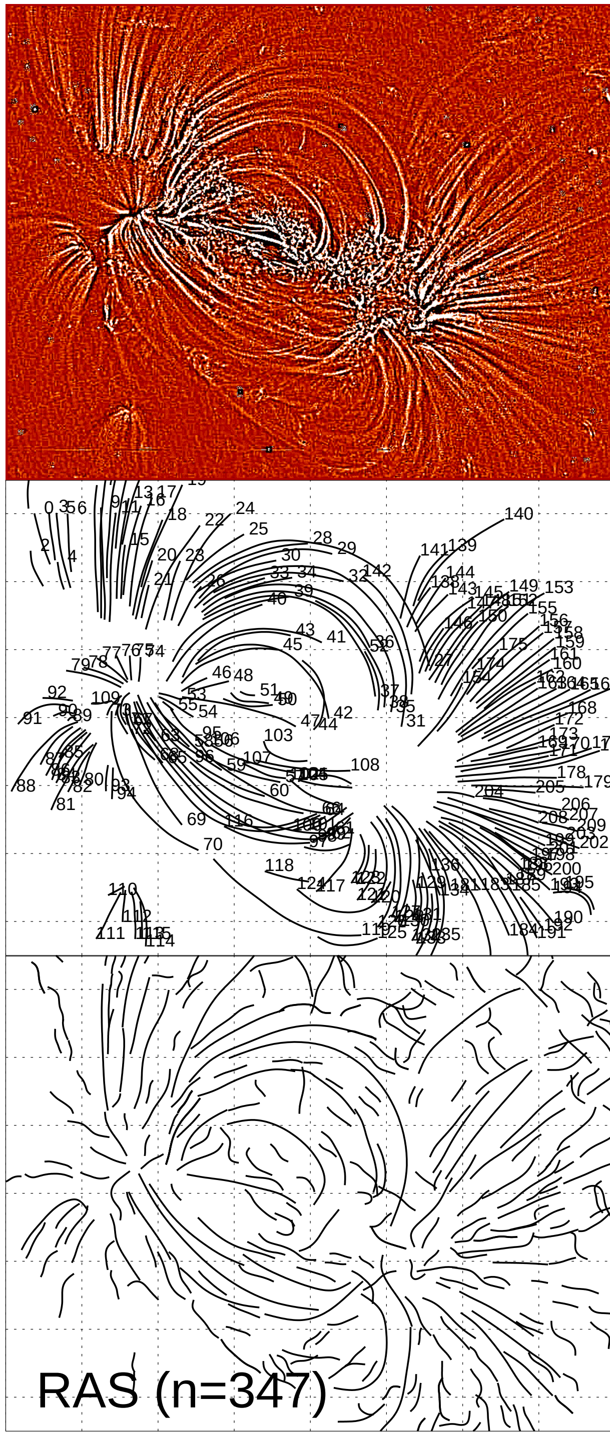

Figure 5. Highpass-filtered partial TRACE image observed on 1998 May 19, 22:21 UT (top), with 210 manually traced loop structures (middle), and 347 automatically traced loop segments using the ridge detection by automated scaling (RAS) code of Inhester et al. (2007) [adapted from Aschwanden et al. 2008a].

3.1. Curvi-linear (1D) Feature Detection

Since the solar corona is permeated by a magnetic field that has a low plasma β-parameter (i.e., the magnetic pressure is much higher than the thermal pressure), the coronal plasma can only flow along the magnetic field lines and thus displays essentially one-dimensional structures, such as coronal loops, postflare loops, filaments, or prominence threads. In principle, automated detection algorithms for one-dimensional structures exist also in medicine (for detecting blood arteries or tumors), in geology (for detecting geological layers in icecores), or in geography (for tracing roads, railways, or rivers in photogrammetric and remote-sensing images from satellites and airplanes), but solar features have quite different properties regarding contrast, background, confusion, intersections, bifurcations, clustering, curvatures, etc., so that each existing code has to be customized and trained specifically to solar features.

Most detection algorithms of curvi-linear features use highpass-filtered images and detect curvi-linear segments using a suitable threshold criterion. The detected curvi-linear segments have first a 2D "island" shape (i.e., image segmentation), which are reduced to 1D structures by detecting the highest ridge line using a pixel-to-pixel gradient criterion. The so-detected 1D segments are then improved by connecting contiguous segments across intersections (with matching directivity) and by smoothing of their local curvature radii. Such basic "oriented-connectivity" codes have been developed for detection of coronal loops in EUV images by Lee et al. (2004, 2006a,b), Aschwanden (2008a), Smith (2005), and Inhester et al. (2008). The directivity of traced loops can additionally be guided by a priori knowledge of a magnetic field model (Lee et al. 2004) and by the cross-sectional geometric properties of loops (Lee et al. 2006a,b; Smith 2005; Inhester et al. 2008) [for an example of the latter code see Fig. 5). A quantitative comparison of five such automated loop tracing codes is carried out in Aschwanden et al. (2008a). Newer developments include detection of elliptical loop geometries with the incremental Hough transform (Sellah and Nasraoui 2008) or supervised (neural) learning strategies based on classifiers, such as RIPPER, Multi-Layer Perceptron, or Adaboost (Durak et al. 2009; Durak and Nasraoui 2009).

The automated detection of curvi-linear structures in the solar corona is most useful for 3D reconstruction of the coronal magnetic field with stereoscopy (e.g., Feng et al. 2007) and for testing theoretical magnetic field models (e.g., potential fields, linear, or nonlinear force-free fields, etc.; DeRosa et al. 2009; Sandman et al. 2009), because they represent independent tracers of the magnetic field.

3.2. Region-based (2D) Feature Detection

Some of the oldest features traced on the Sun were sunspots, starting with Galileo's famous drawings around 1610. Sunspot drawings were continuously recorded at the 150-foot solar tower telescope on Mount Wilson over the last century (1917-2007). The morphological shape of sunspots was systematically classified by a scheme devised by Max Waldmeier in 1938, called the *Zürich method of sunspot classification*. The Zürich sunspot group classification was later generalized, including up to 60 distinct types of sunspot groups (McIntosh

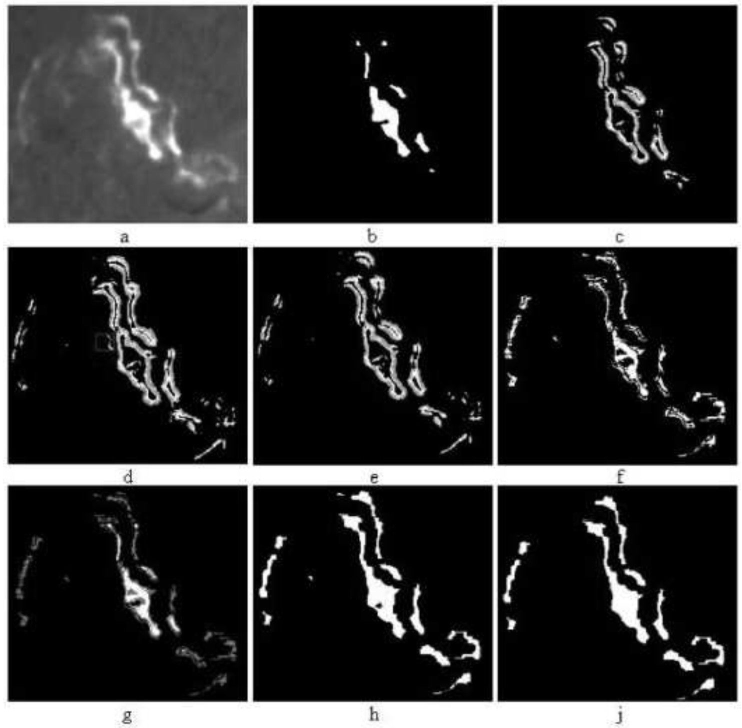

Figure 6. Examples of some mathematical morphology operators used in region-based 2D feature recognition: (a) Original image recorded in Hα from Big Bear Solar Observatory (BBSO), (b) result of the region growing operator, (c) result of the global threshold boundary method, (d) result of the adaptive threshold boundary method, (e) result of the improved adaptive threshold method, (f) result of the boundary growing method, (g) result of the region growing plus the boundary growing method, (h) result of the morphological closing, (i) result of the small part removing and hole filling [from Qu et al. 2004].

1990). Naturally, with increasing amounts of digital solar images the motivation for automated detection and classification did arise, in order to model the total solar irradiance in an objective way. First automated codes were applied to photometrically calibrated optical images, using a detection criterion based on contrast (threshold) and contiguity, after the limb was fitted and the center-limb profile of the background was subtracted (Preminger et al. 2001). A comparison of various automated feature classification methods with the Mount Willson classification was carried out by Jones et al. (2008, 2009). The exact determination of the ragged contours of a sunspot, active region, or filament area is generally accomplished with so-called *region-based feature recognition methods* (Zharkova et al. 2003, 2005a,b,c, Zharkova and Jain 2007). Such methods entail iterative steps of *mathematical morphology operators* (such as thresholding, segmentation, labeling, symmetric difference, dilation, erosion, filling with a watershed function, region-growing, opening, closing, hit-or-miss transform, top-hat transform, granulometry, thinning, skeletonization, skeleton pruning, ultimate erosion, conditional bisector, etc., see Table 3 for descriptions). Some examples of such data manipulations are shown in Fig. 6.

Table 3. Mathematical morphology operators applied to 2D (area) features

Operator	Description
Labeling	assign a unique value to pixels belonging to the same connected region in a binary image
Symmetrical difference	difference area between the combined (union) and overlapping (intersection) area of 2 features
Dilation	convolution of a feature with a kernel function
Erosion	rounding the ragged boundaries of a feature
Morphological gradient	subtract erosion from dilatation of a feature
Distance transform	maps distance from border of its connected component
Opening	composition of an erosion followed by a dilation
Closing	composition of a dilation followed by an erosion
Conditional dilation	overlap between dilated image and conditional image
Close holes	fills holes in every connected component
Hit-miss	intersection of an erosion and an anti-dilation
Thinning	subtraction between input and sup-generating operator
Thickening	union of input image and sup-generating operator
Skeleton by thinning	iterative thinning by successive rotation of pattern
Wathershed	simulating a flood on a surface to find wathersheds

Such mathematical morphology methods have been applied to a number of automated tasks: to measure sunspot areas and active region sizes in magnetograms (Zharkov et al. 2005a,b; McAteer et al. 2005), and white-light solar images (Curto et al. 2008), to catalog active regions and filaments in Hα and Ca II images (Shih and Kowalski 2003; Benkhalil et al. 2006; Fuller et al. 2005; Bernasconi et al. 2005) and SOHO/EIT images (Scholl and Habbal 2008), to identify the chirality and magnetic field inversion in filaments (Bernasconi et al. 2005; Ipson et al. 2005, 2009), to measure the magnetic helicity injection of flaring active regions (LaBonte et al. 2007), for active region identification and magnetic field disambiguation (Georgoulis et al. 2008), to deduce the magnetic tilts and charge separation in sunspot groups (Zharkova and Zharkov 2008), to quantify the phase relation between toroidal (sunspot) and poloidal (background) magnetic field (Zharkov et al. 2008), to quantify the role of the Wilson depression in sunspot detection (Watson et al. 2009), to off-limb detection of EUV prominences (Foullon and Verwichte 2006), to detect sigmoids in full-disk soft X-ray images (Bernasconi and Georgoulis 2009), or to detect coronal holes (Krista and Gallagher 2009; Scholl and Habbal 2008).

3.3. Spectral Methods of Feature Detection

Similar to Fourier or wavelet analysis of time series data, spatial images can be decomposed into spatial Fourier components in form of a power spectrum, which we thus call a *spectral method* of image analysis. A spectral decomposition of spatial scales in an image is just an equivalent representation of the same image information in a different parameter space, namely in Fourier space, and can be back-transformed to retrieve the same original image. In analogy to wavelet analysis in the time domain, where the wavelet transform gives information on both time periods as well as the relevant time intervals where each period dominates, the wavelet transform in the spatial domain provides information on both spatial length scales as well as on their local positions (in the image) where they occur. It is therefore a useful method for feature detection (of a selected length scale) or for image compression algorithms (that take advantage of eliminating data noise that is contained in the shortest length scales). If a power spectrum of spatial scales fits a powerlaw function, it can be characterized by its slope, which is related to the *fractal dimension*, and in a generalized fashion, multiple powerlaw slopes lead to *multi-fractal analysis*. An introduction into feature recognition and classification using spectral methods can be found in Section 5 (by K. Revathy) in Zharkova and Jain (2007).

Let us review some applications of spectral feature detection in solar data (see also Table 2). A wavelet analysis applied to magnetograms revealed dominant power in structures of length scales corresponding to the supergranulation and mesogranulation (Komm 1994) and a fractal dimension of $D_f = 1.7$ (Komm 1995). A related technique is the *Hurst's rescaled range analysis*, which quantifies a Hurst exponent (powerlaw index) of the distribution of fluctuations in a range (here in length scales) normalized by the range, and can be used to characterize the complexity of an active region (Adams et al. 1997). Two fractal methods (the differential box counting and the Jaenisch scheme) were also used to characterize the complexity of magnetograms (Stark et al. 1997). Multifractal analysis of solar magnetograms was employed to discriminate between flaring and non-flaring active regions (Abramenko 2005), or to detect turbulence for flare prediction (Georgoulis 2005, 2009). Systematic changes in the multi-fractal dimension of active regions were detected during emergence, and a relationship between the multi-fractal properties for the flaring regions and their flaring rate was found (Conlon et al. 2008; Hewett et al. 2008), as well as between the Mt. Wilson sunspot classification and flaring activity (Ireland et al. 2008).

A wavelet transform (the *á trous algorithm*) was applied to SOHO/EIT images to enhance hidden loop and filament features above the noise level (Portier-Fozzani et al. 2001). The *singular spectrum analysis (SSA)* method uses fixed basis functions (as in the case for Fourier or wavelet transforms), based on the *Principal Component Analysis*, which performs an eigenvalue-eigenvector decomposition of a one-dimensional dataset, and was applied to azimuthal limb profiles to detect sunspots and faculae (Lefebvre and Rozelot 2004). To enable a non-subjective segmentation of photospheric and chromospheric features, a *multi-scale Laplacian-of-Gaussian operator* and an iterative version of the *medial axis transform* was applied to photospheric Doppler images (Berrilli et al. 2005). A fractal-based fuzzy segmentation technique was developed to extract active regions (Revathy et al. 2005).

3.4. Artificial Intelligence in Feature Detection

Now we turn to a more complex class of automated feature detection algorithms, which include the capability of *neural network learning*. The term *neural network*

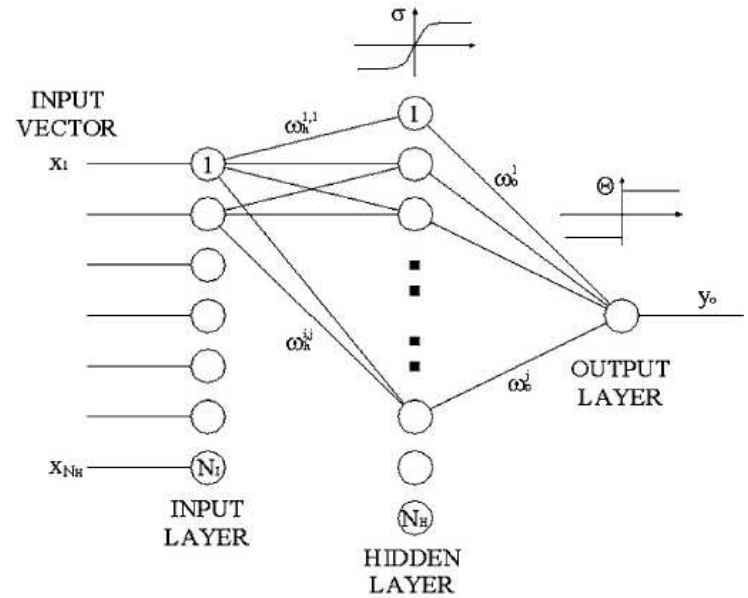

Figure 7. The architecture of a neural network algorithm [Fernandez Borda et al. 2002].

originally referred to a network of biological neurons, but is now called *artificial neural networks* or *artificial intelligence* in computational mathematics. The essential aspect is that learning is accomplished by the mutual interactions between many different neurons (which are connected with other neurons by synapses in the brain). The mathematical algorithms of artificial intelligence try so simulate these interactions between neurons, which can be described by a learning process involving three layers (input layer, hidden layer, and output layer) (Fig. 7). For instance, let us consider the classification of sunspots. The input layer consists of p characterizing parameters of a newly observed sunspot image (say the area, circumference, mean brightness, standard deviation of brightness, etc.), which are then inter-compared with a set of master examples of previously classified sunspots (say n classes A, B, C, ...) labelled by an expert. The range of each parameter p is not exactly defined for each class, but has to be narrowed down from probability distributions in each class. This is the essential training or learning process, to derive parameter combinations (classifiers) that are most discriminant between the different classes, and thus can be used to classify most accurately a new observation. Some parameters may be irrelevant, and thus degrade the classification accuracy, while other parameters are redundant, and thus are useless. So, the artificial intelligence algorithm will find the best combination of parameters that is most efficient and accurate for a classification. After a classification model has been deduced from the training data set, the classification scheme has to be validated by a disjoint set of test data to verify the consistency and accuracy of the classification scheme. An introduction into feature recognition and classification based on artificial intelligence can be found in Section 4 of Zharkova and Jain (2007).

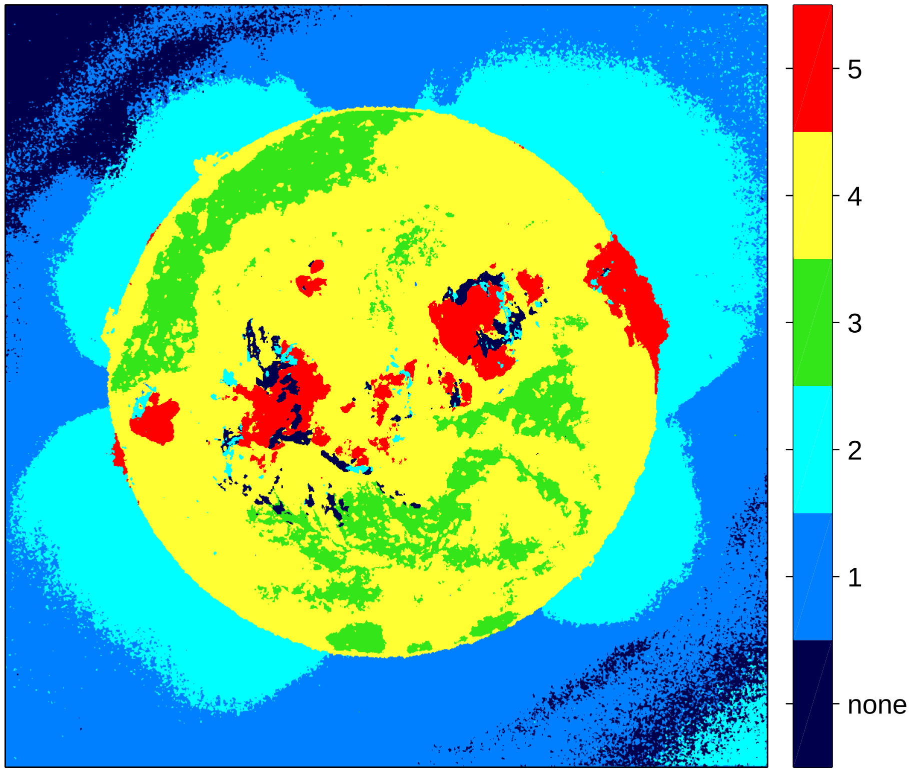

Figure 8. Example of segmentation of a SOHO/EIT 171 Å image and automated labelling of 5 classes using an artificial intelligence algorithm. The 5 classes are (see color scale on right-hand side): (1) tenuous off-limb corona, (2) dense off-limb corona, (3) coronal holes, (4) quiet sun, (5) active regions [De Wit 2006].

Artificial intelligence can be applied to any of the three previously described groups of pattern recognition algorithms, i.e., curvi-linear 1D feature detection (§3.1), region-based 2D feature detection (§3.2), or spectral methods of feature detection (§3.3), so it constitutes just a higher level of data manipulation that involves neural network learning. For solar data, artificial intelligence algorithms in feature recognition have been applied to SOHO/MDI magnetograms to automatically classify quiet Sun, faculae, sunspots (umbra and penumbra) features (Turmon et al. 2002) or the McIntosh-based sunspot classification (Colak and Qahwaji 2008), to Hα spectroheliograms to detect filaments (Zharkova and Schetinin 2005), to Stokes profiles to extract a small subset of parameters that can reconstruct the original profile (Socas-Navarro 2005a,b), to SOHO/EIT images to obtain a fast segmentation with classification into coronal holes, quiet Sun, active regions (Fig. 8; De Wit 2006), using multi-spectral images (De Wit et al. 2009), to TRACE images to automatically detect coronal loops using supervised neural learning strategies based on classifiers, such as RIPPER, Multi-Layer Perceptron, or Adaboost (Durak et al. 2009; Durak and Nasraoui 2009), or to SOHO/EIT and STEREO/EUVI images to automatically detect prominences above the limb using a support vector machine (SVM) technique (Labrosse et al. 2009).

4. Automated Detection and Tracking of Features in Time

While we dealt with recognition of *spatial features* in the last Section, usually applied to a single 2D image, we are exploring now feature recognition in the *time domain*, either applied to a simple 1D time series $f(t)$, a 2D space-time slice $f(x,t)$, or a 3D data cube (movie) $f(x,y,t)$. In principle, the same already discussed feature recognition codes applied to 2D images $f(x,y)$ could be executed in a 3D data cube $f(x,y,t=t_i)$ for every time t_i, $i=1,...,n$ individually, but since every motion or temporal evolution $[x(t),y(t)]$ has some correlated behavior in time, it is more efficient to track features in time by taking advantage of time-coherent functions in the detection algorithm, such as used in *threshold-based detection* (§4.1), *principal component analysis* (§4.2), *Fourier or wavelet transform* (§4.3), *Hough transform* (§4.4), *local correlation tracking method* (§4.5), and related *artificial intelligence algorithms* (§4.6). To clarify the semantics we will refer to *temporal features* briefly as *events*, and correspondingly, *event catalogs* entail lists of temporal features. A list of event detection algorithms applied to solar data is provided in Table 4.

4.1. Threshold-Based Detection of Temporal Features

The simplest method of automated detection of temporal features is based on a threshold criterion, e.g., when an observed parameter (e.g., flux, intensity, or area) of a time profile or data cube exceeds some minimum threshold value above the noise level, after proper calibration and elimination of spatio-temporal variable background components. The beginning and the end of an event is simply defined by the time interval when the selected parameter (i.e., flux or geometric area) contiguously exceeds a predefined threshold value. Such algorithms are used for automated detection of solar flares, CMEs, eruptive filaments, nanoflares, etc., in order to create catalogs of events, to obtain statistical distributions, or to enable real-time forecasting. We mention a few examples of such automated detection algorithms in the following.

Statistics and frequency distributions of nanoflares down to the data noise level was gathered by threshold-based detection of brightness increases clustered in space and time in EUV image data cubes from SOHO/EIT (Krucker and Benz 1998) and TRACE (Parnell and Jupp 2000; Aschwanden et al. 2000b). Statistics of 10^9 EUV bright points over 9 years was obtained by detecting significant brightenings above a background flux level in full-disk SOHO/EIT images (McIntosh and Gurman 2005). The emergence and evolution of small kilo-Gauss fields in the photosphere was automatically detected and tracked in high-resolution *SST* image data cubes (Crockett et al. 2009). Ten times more dynamic Hα features (surges, filament activations) were detected with a threshold-based automated method than by visual identification (Liu et al. 2005). Automated flare detection was accomplished with region-based and edge-based image segmentation of Hα image data cubes (Veronig et al. 2000). Automated detection

Table 4. Automated Detection Algorithms applied to Solar Events (Temporal Features): N=Nanoflares, B=Bright points, F=Flares, C=CMEs, F=Eruptive filaments, O=Oscillating Loops, W=Propagating Waves, M=magnetic field, P=plumes, G=Granulation

Event Detection Algorithm	N	B	F	C	D	O	W	M	P	G
Threshold-based detection of events										
(1) Flux threshold, spatio-temporal clustering	N									
(2) Significant brightenings, intensity threshold		B								
(3) Region-based and edge-based image segmentation			F							
(4) Dark intensity threshold, time slices			F							
(5) Radial off-limb images, threshold segmentation				C						
(6) Base-line subtracted lower-envelope images					D					
(7) Flux threshold, propagating ring patterns							W			
(8) Intensity thresholding, compass search								M		
Principal component analysis (PCA)										
(9) Principal component analysis								M		
(10) Complex empirical orthogonal function								M		
(11) PCA, Independent component analysis								M		
(12) Proper orthogonal decomposition analysis								M		
Fourier, wavelets, spectral methods										
(13) Power spectra, autocorrelation								M		
(14) Multiple level tracking algorithm										G
(15) Multiple-scale pattern recognition										G
(16) Wavelet, Hölder exponent	N									
(17) Fractal analysis in time								M		
(18) Continuous wavelet transform								M		
(19) Structure function, multi-fractals								M		
(20) á Trous wavelet transform						O				
(21) Morelet wavelet analysis						O				
(22) Power spectra, pixelized wavelet filtering						O	W			
(23) Bayesian spectral analysis						O				
(24) Multi-scale edge detection, wavelets				C						
Hough transform										
(25) Morphological opening, Hough transform				C						
(26) Continuous and Mexican Hat wavelet, Hough transform									P	
Local correlation tracking (LCT) methods										
(27) LCT, horizontal flows, vertical vorticity									M	G
(28) LCT, multi-scale elastic matching										G
(29) Tracker particles, time-reversed flow field										G
(30) Coherent structure tracking (CST)										G
(31) COLIBRI code, detect lineaments or contours										G
(32) Fourier local correlation tracing										G
(33) Comparison of LCT codes									P	G
(34) Edge enhancement, curvature determination								M		
(35) Coherence-based travel-time tracking						O				
(36) Multi-scale optical flow (Velociraptor code)			F			O				
(37) LCT, stereoscopic images	A					L				
Artificial intelligence in event detection										
(38) Two layers, back-propagation algorithm			F							
(39) MLP, RBF, SVM algorithms		C	F	E						
(40) Unsupervised fuzzy clustering algorithm	AQH									
(41) Support vector machine (SVP) algorithm		C								

Table 4.

References: 1 (N): Krucker and Benz (1998), Parnell and Jupp (2000), Aschwanden and Parnell (2002); 2 (B): McIntosh and Gurman (2005); 3 (F): Veronig et al. (2000); 4 (F): Liu et al. (2005); 5 (C): Olmedo et al. (2008); 6 (D): Aschwanden et al. (2009b); 7 (W): Podladchikova and Berghmans (2005); 8 (M): Crockett et al. (2009); 9 (M): Lawrence et al. (2004); 10 (M): Terradas et al. (2004); 11 (M): Cadavid et al. (2008); 12 (M): Vecchio et al. (2005a,b, 2008); 13 (M): Ulrich (2001); 14 (G): Bovelet and Wiehr (2001); 15 (G): Bovelet and Wiehr (2007); 16 (N): Delouille et al. (2005, 2008); 17 (M): Criscuoli et al. (2007); 18 (M): Hewett et al. (2008); 19 (M): Salakhutdinova and Golovko (2004), Abramenko (2005), Georgoulis (2005, 2009); 20 (O): Katsiyannis et al. (2005); 21 (O,W): Jess et al. (2007, 2008); 22 (O): Nakariakov and King (2007), Sych and Nakariakov (2008), Sych et al. (2009a,b), DeMoortel and McAteer (2004); 23 (O): Ireland et al. (2009); 24 (C): Young and Gallagher (2008), Byrne et al. (2009); 25 (C): Robbrecht and Berghmans (2004), Robbrecht (2007), Robbrecht et al. (2009); 26 (P): De Patoul et al. (2009); 27 (G): November et al. (1981), Simon et al. (1994), Hagenaar et al. (1997, 1999, 2003), Hagenaar and Shine (2005), Berger et al. (1998), Shine et al. (2000); 28 (G): Collin and Nesme-Ribes (1995); 29 (G): Potts et al. (2003, 2004), Potts and Diver (2008); 30 (G): Rieutord et al. (2007), Tkaczuk et al. (2007); 31 (G): Getling and Buchnev (2008); 32 (G): Balthasar and Muglach (2009); 33 (G): DeForest et al. (2007), Chae (2008); 34 (M): Hamedivafa (2008); 35 (O): McIntosh et al. (2008); 36 (O,F): Gissot and Hochedez (2007, 2008), Gissot et al. (2008); 37 (A,L): Rodriguez et al. (2009); 38 (F): Fernandez Borda et al. (2002); 39 (F): Qu et al. (2003, 2004, 2005, 2006); 40 (A,Q,H): Barra et al. (2008); 41 (C): Olmedo et al. (2009).

and tracking of CMEs in coronagraph time series with the SEEDS code applied to LASCO data successfully detects 75% of CME events recorded in the CDAW catalog (Olmedo et al. 2008). Automated tracking of EIT waves in SOHO/EIT images was tested with flux threshold-based detection of spherically propagating ring patterns (Podladchikova and Berghmans 2005). Automated detection of EUV dimming is accomplished most efficiently from threshold-based lower envelopes in pre-CME baseline-subtracted EUV images with suppression of brightening postflare loops (Aschwanden et al. 2009b).

4.2. Principal Component Analysis

Principal Component Analysis (PCA) is a statistical procedure that transforms a number of possibly correlated variables into a minimum number of uncorrelated (independent, or orthogonal) variables, which are called *principal components* or *proper orthogonal decomposition*. The PCA procedure can be used for automated detection of spatial or temporal features. Applied to time series analysis, it can reveal dominant time periods, in some more general way than Fourier or wavelet transforms (which are sensitive to periodic signals only). The detection of intervals with a dominant time period essentially constitutes the detection of an event, because its duration corresponds to a local time period or principal component.

Regarding solar feature detection, a principal component analysis was applied to synoptic maps of NSO Kitt Peak magnetograms in order to find an optimal represenation of the axisymmetric magnetic field during the solar cycle over the last 350 years (Lawrence et al. 2004). A *complex empirical orthogonal function* method was employed to identify the wavelengths and periods of propagating acoustic waves in coronal fan loop structures (Terradas et al. 2004). A PCA and independent component analysis (ICA) was used to identfy global patterns in the interplanetary magnetic field polarity at 1 AU in *Wind* and *ACE* data (Cadavid et al. 2008). A proper orthogonal decomposition analysis was used to quantify the butterfly diagram of solar activity in the green coronal emission line (5303 Å) (Vecchio et al. 2005b) or to identify low-frequency oscillations in photospheric motion (Vecchio et al. 2005a, 2008).

4.3. Fourier and Wavelet Methods

A classic method of time series analysis is the *Fourier transform method*, or the *Windowed Fourier Transform*, also called *Wavelet Analysis* or *multi-resolution analysis*, which all fall into the category of *Spectral Methods*. The Fourier method is most suitable for periodic modulations, especially if a dominant period persists over the entire analyzed time interval. In reality, however, periodic phenomena may switch on or off at arbitrary times during the analyzed time interval, for which a wavelet analysis is more useful, because it can detect periodic signals in any sub-interval (or "time window"), and for that reason has been dubbed *Windowed Fourier Transform*. In the absence of periodic signals, there will be no peaks in the power spectrum, but just a monotonic decrease of power towards higher frequencies. However, even the slope of a power spectrum can reveal significant physical information, such as 1/f-noise, white noise, red or brown noise, black noise, turbulence, powerlaw behavior (implying self-organized criticality and fractal dimensions), or multi-powerlaw behavior (implying multi-fractals). A quantity related to power specra is the *structure function*, which is used to characterize turbulent flows. Numerical recipes for Fourier transform and spectral methods can be found in Press et al. (1986).

In the following we review recent studies that employed such spectral methods in the time domain in automated feature recognition algorithms applied to solar data. Very long-lived wave patterns in the solar surface velocity signals were detected by power spectra and autocorrelation (Ulrich 2001), which is related to the many applications of spectral methods used in helioseismology (which is beyond the scope of this review). The time evolution and fractal dimension of granulation and limb faculae features was tracked with a multiple level tracking algorithm, superior to commonly used Fourier-based recognition techniques (Bovelet and Wiehr 2001). Faint intergranular G-band structures at very high resolution were studied with a multiple-scale pattern recognition code (Fig. 9) and compared with Ca II H enhancements (Bovelet and Wiehr 2007). The preflare activity was monitored with the time evolution of structure functions and their scaling parameters in Hα images, which revealed intermittent turbulence and multi-fractal structures (Salakhutdinova and Golovko 2004). A similar multi-fractal analysis on SOHO/MDI magnetograms revealed that flare-quiet active regions possess a lower degree of multi-fractality than flaring active regions (Abramenko 2005), and similarly in SOHO/EIT images (Georgoulis 2005, 2009). The multiscale structure of an evolving active region analyzed with a continuous wavelet technique displayed an energy spectrum that is consistent with an inverse turbulent cascade (Hewett et al. 2008). A gradient pattern analysis and discrete wavelet

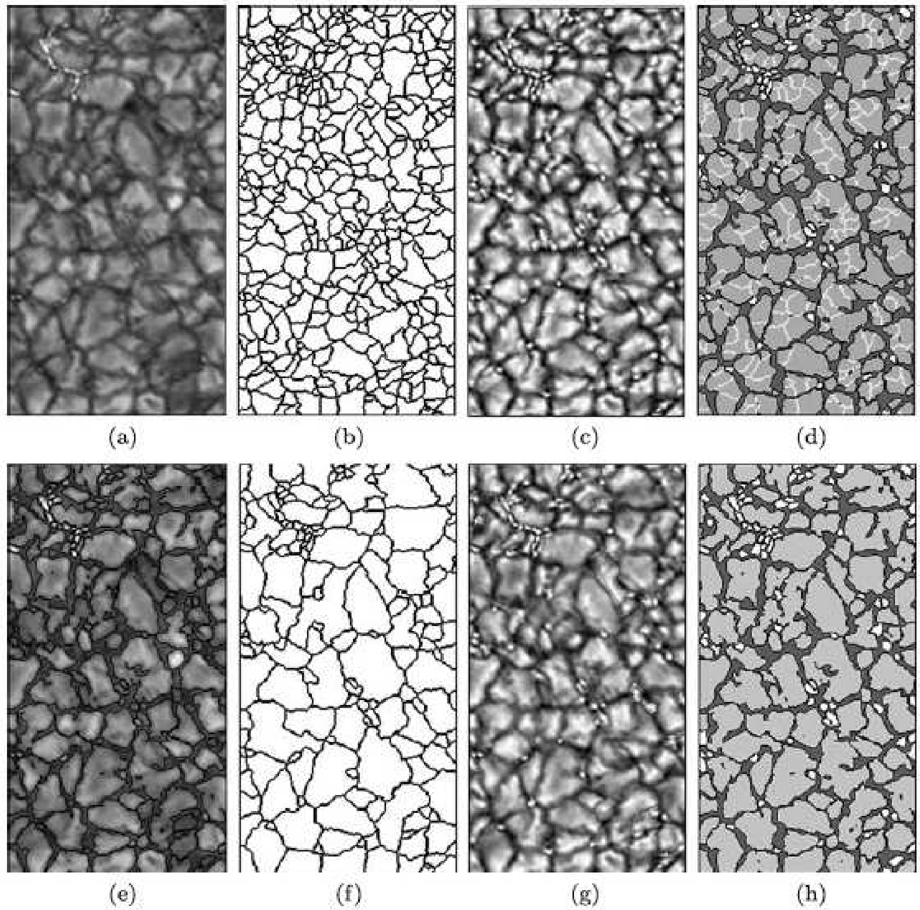

Figure 9. Demonstration of subsequent phases of the MLT_4 procedure for a reconstructed disk center G-band image (19 October 2005; DOT). (a) $24.1'' \times 12.6''$ subfield; (b) phase 1: pattern of segmented "cells" as detected by multiple level pattern recognition using 20 intensity thresholds; (c) phase 2: intensity normalization for each segmented cell; (d) phase 3: shrunk features (gray) after unitary cut, with features excluded from merging marked white; (e) phase 4: final pattern (black contour pixels), with the division lines (light gray) now removed; (f) expansion of the final features to a cellular pattern; (g) intensity normalization for these cells; (h) selection of particular features, here small intergranular structures (white) [Bovelet and Wiehr 2007].

decomposition analysis of short solar radio bursts was also found to be consistent with an intermittent and strong MHD turbulent variability pattern (Rosa et al. 2008). During a solar cycle, however, the fractal and multi-fractal properties of magnetic features were found not to vary significantly (Criscuoli et al. 2007). Spatial (sub-pixel) and temporal noise in EIT images, which potentially could hide nanoflare activity, was investigated with a wavelet analysis (Delouille et al. 2005) and with a pointwise Hölder exponent analysis (Delouille et al. 2008).

High-frequency oscillations in Hα and G-band images of sunspots were found with a Morelet wavelet analysis (Jess et al. 2007). The search for coronal waves

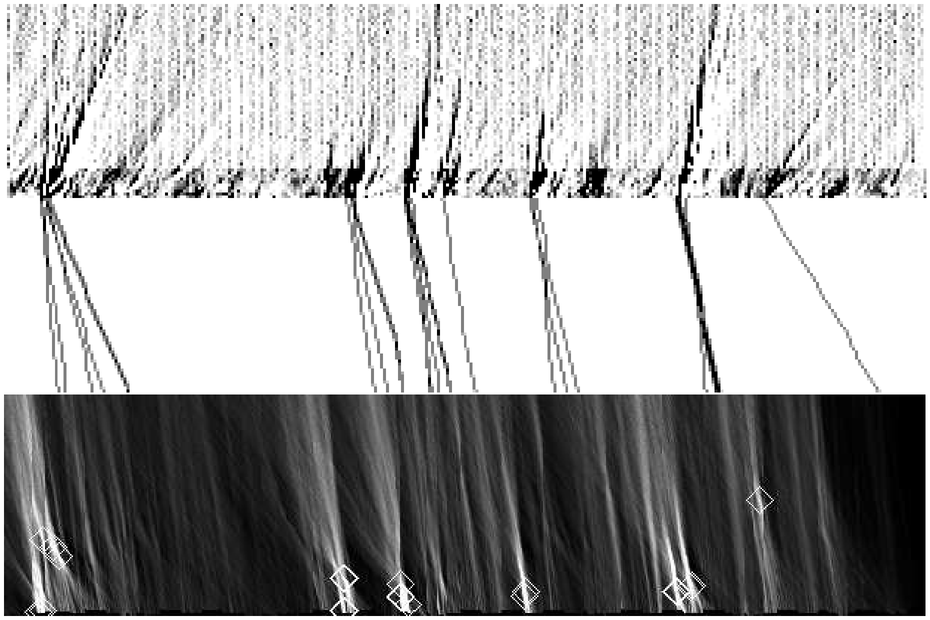

Figure 10. Example of a height-time plot of white-light intensity in radial direction above the limb from SOHO/LASCO/C2+C3 during 2003 November 9-14 (top). The Hough transform extracts a signal for diagonal straight lines (bottom), where the inclination angle of the ridges corresponds to the CME propagation velocity. The corresponding ridges are shown upside down (middle) [Robbrecht and Berghmans 2005; Robbrecht 2007].

during the solar eclipse 2001 observed with SECIS (recording 8000 pictures) was conducted with the *á Trous wavelet transform*, but no clear oscillatory signal was found (Katsiyannis et al. 2005). Coronal loop (kink-mode) oscillations were analyzed with an automated edge-tracking algorithm and with the Morlet wavelet transform, which confirmed the transverse kink-mode oscillations but found also spatial periodicities along the loop (Jess et al. 2008). A systematic tool that automatically detects wave and oscillatory phenomena in coronal data in form of *coronal periodmaps* was developed using power spectra (Nakariakov and King 2007) and pixelized wavelet filtering (Sych and Nakariakov 2008; Sych et al. 2009b; DeMoortel and McAteer 2004; Ofman et al. 2009), applied to TRACE images. Simultaneous wavelet analysis in sunspots and 17 GHz microwaves even revealed that 3-min oscillations leaking out from sunspots can trigger oscillations in coronal (radio-emitting) flare loops (Sych et al. 2009a). Another automated detection code of oscillating regions was developed based on Bayesian spectral analysis, which identifies first time intervals (Bayesian time blocks) with high probability for oscillations at every spatial location (Ireland et al. 2009).

Also automated detection of CMEs is now accomplished with multi-scale and wavelet techniques, e.g., using a multi-scale edge detection technique applied to SOHO/LASCO and TRACE data (Young and Gallagher 2008), which allows also to enhance the visibility of faint CMEs and to track the kinematics (height, velocity, acceleration vs. time) of CMEs (Byrne et al. 2009).

4.4. Hough Transform

The Hough transform is a particular multi-dimensional feature detection algorithm that is specialized for the detection of straight lines, circles, and ellipses. It was originally introduced and patented by Paul Hough in 1962, and an introduction of the Hough transform for robust regression and automated detection can be found in Ballester (1994). In solar physics, the Hough transform was primarily applied to automated detection of straight lines (diagonal-like) in 2D distance-time diagrams, such as the height $h(t)$ of the leading edge of a propagating CME as function of time, which follows a straight line for a constant velocity. The required preprocessing for this method requires the extraction of the height (i.e., radial wedge from Sun center at a given position angle), which has to be assembled from a 3D data cube in form of a 2D time-slice plot $h(t)$ (Fig. 10).

A first automated CME detection code using the Hough Transform was developed by Robbrecht and Berghmans (2004), which identified CMEs from near-real-time LASCO data with an overall success rate of $\approx 94\%$. The feature detection is based on clustering and a morphological closing operator, and the output is a CME list that contains starting time, position angle, angular width, and velocity of the bright CME front (Robbrecht and Berghmans 2004, Robbrecht 2007). Statistics based on this first automatically constructed LASCO CME catalog, using the so-called *CACTUS* code, revealed an invariant angle range during a solar cycle and a powerlaw distribution of CME sizes (Robbrecht et al. 2009). For reliable space weather predictions, the automated detection of various CME features and precursors, such as disappearing filaments in Hα images, EUV dimming, EIT or global waves, erupting prominences in radio images, and CME fronts seen in coronagraph white-light images, need to be combined in order to achieve optimum reliability (Robbrecht and Berghmans 2005). The Hough transform was also used to reconstruct the 3D geometry of coronal polar plumes (De Patoul et al. 2009).

4.5. Local Correlation-Tracking Methods

For features that vary their morphological shape slowly with time (with respect to the observing cadence of the images), their geometric shape is highly correlated in subsequent time frames, and thus *local correlation tracking methods* are most suitable for tracing their time evolution. Examples of such phenomena are the magneto-convection of photospheric granulation cells, chromospheric flows seen in Hα, chromospheric evaporation in postflare loops, shrinking and expanding coronal loops, or the expansion of CME shells. The trajectories of these motions can often be predicted to first order from previous frames, which helps to lock in local correlation techniques to corresponding structures. We give a few examples of such local correlation-tracking methods and their applications to solar phenomena in the following.

Local correlation tracking (LCT) methods were applied to high-resolution data cubes of photospheric granulation features to produce flow maps. From the horizontal flow velocity $\mathbf{u}_H$ one can compute the horizontal divergence, $\Delta = \nabla \cdot \mathbf{u}_H$, and the vertical component of the vorticity, $\nabla \times \mathbf{u}_H = \omega \hat{\mathbf{z}}$, which allows

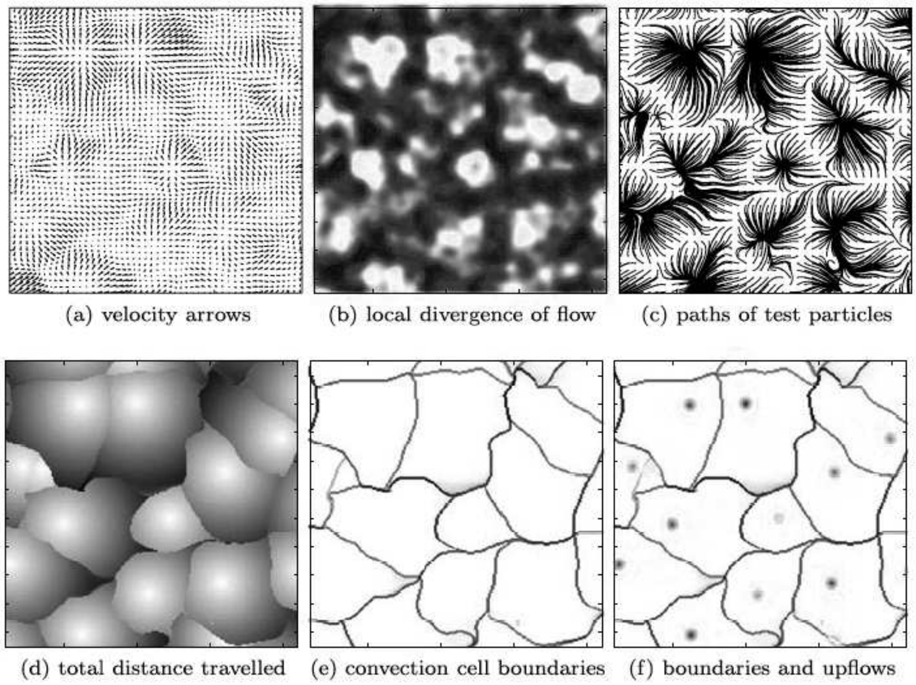

Figure 11. Example of a balltrack analysis (using a watershed algorithm) to identify supergranular cell boundaries. The data shown are a 90×90 Mm region near disk center under quiet-Sun conditions. The velocity field is averaged over 3 hrs and spatially moothed by convolution with a 2D Gaussian with radius of 1.75 Mm [Potts and Diver 2008].

to derive outflows, inflows, vortex motions, lifetimes, sizes, shapes, motions, and locations of photospheric granules relative to each (Simon et al. 1994). The LCT technique applied to larger field of views revealed supergranulation and meso-granulation structures (November et al. 1981; Shine et al. 2000). Early applications of LCT algorithms measured the magnetic element motion from (La Palma) high-resolution filtergrams (Berger et al. 1998). A noise-resistant method for automated identification of supergranular cell boundaries from photospheric velocity measurements was developed, applied to SOHO/MDI images, and shows emergence, splitting, coalescence, and lifetimes of supergranular cells (Fig. 11; Potts et al. 2003, 2004, Potts and Diver 2008). A variant is the *coherent structure tracking (CST)* method, which employs image segmentation, wavelet analysis of the flow field, and computation of the field derivatives like the horizontal divergence and vertical vorticity (Rieutord et al. 2007; Tkaczuk et al. 2007). Evidence for roll convection in granulation data was inferred from the widespread occurrence of ridges and trenching patterns detected in lineaments or contours of photospheric images (Getling and Buchnev 2008). A LCT code with multi-scaling elastic matching allows extracting and tracking of magnetic features, and to derive rotational and meridional motions with high accuracy (Collin and Nesme-Ribes 1995). Local correlation tracking of small moving magnetic features around sunspots revealed lifetimes of ≈ 1 hr, initial velocities of $v \approx 1.8$ km s^{-1}, and magnetic fluxes of $\Phi \approx 2.5 \times 10^{18}$ Mx (Hagenaar et al. 1997, 1999, 2003, Hagenaar and Shine 2005). Umbral dots with sizes 230 km were automatically identified and tracked with an edge enhancement and curvature determination algorithm (Hamedivafa 2008). LCT conducted in sunspot moats in whitelight and UV tracks the 3D moat flow in different heights (Balthasar and Muglach 2009). A comparison of 4 LCT tracking codes applied to the same SOHO/MDI image has been conducted by DeForest et al. (2007), who makes recommendations for feature selection and tracking practice. A test of 3 optical flow algorithms (LCT, DAVE, NAVE) has also been performed on recent Hinode data of prominences (Chae et al. 2008).

In most recent work, LCT and flow-field tracking was also applied to phenomena in the solar corona. A coherence-based travel-time tracking algorithm demonstrated the automated detection of propagating (sound) waves and standing (kink-mode) oscillations in coronal loops (McIntosh et al. 2008). A multi-scale optical flow method (*Velociraptor algorithm*) was developed to track the motion of erupting filaments (Gissot et al. 2008) or coronal loop oscillations (Gissot and Hochedez 2007, 2008). The 3D reconstruction of active regions was also attempted with STEREO/EUVI data by means of a local correlation tracking method, where corresponding pixels in the two stereoscopic images are automatically matched, a technique that can even be applied to the 3D reconstruction of a single (isolated) coronal loop (Rodriguez et al. 2009).

4.6. Artificial Intelligence in Event Detection

Artificial intelligence algorithm or neural network learning techniques can be trained for automated detection of spatial features (§3.4) as well as temporal features (i.e., events), because the learning algorithms treat all (e.g., spatial or temporal) input parameters equally. Solar applications include automated detection of flare events in full-disk Hα images (Fernandez Borda et al. 2002), using 3 different learning techniques, such as the *muli-layer perceptron (MLP)*, the *radial basis function (RBF)*, and the *support vector machine (SVM)* algorithms (Qu et al. 2003, 2004), extended to detection of filaments, spines, footpoints, filament disappearances (Qu et al. 2005), and CMEs (Qu et al. 2006; Olmedo et al. 2009), and to coronal holes, quiet Sun, and active regions, using a multi-channel unsupervised spatially constrained fuzzy clustering algorithm (Barra et al. 2008).

5. Post-Processing Tasks

After we completed the main data mining steps of automated feature recognition, we are left with an output of numbers, parameters, segmented images, datacubes, and movies that need to be communicated to the scientifically interested audience or research community in a suitable form, by means of visual representation (§5.1), searchable catalogs (§5.2), quantitative statistics (§5.3), input for theoretical modeling (§5.4), or tools for prediction and forecasting

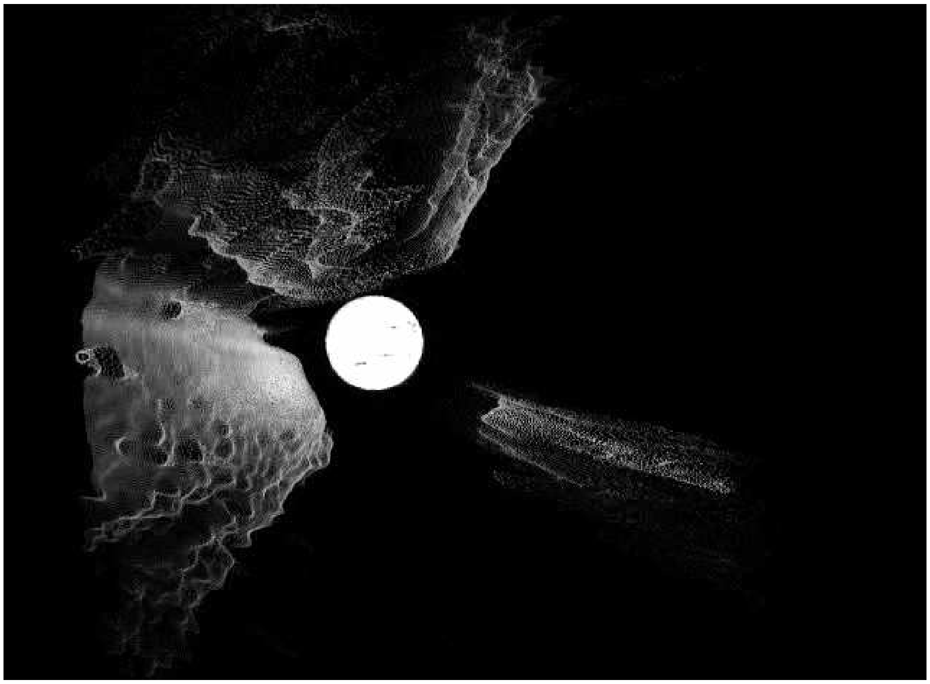

Figure 12. A 3D reconstruction of a CME produced using 2D polarized SOHO/LASCO data analyzed by Moran and Davila (2004) is visualized with a 3D surface illumination technique.

(§5.5). These post-processing tasks are as important as the pre-processing (§2), and main data analysis tasks in terms of automated feature recognition (§3 and 4) to deliver a scientific return.

5.1. Visualization of Solar Imagery

The visualization of solar data started from simple drawings, charts, graphs, diagrams, photographs, color reproductions, but now we record data cubes of multi-wavelength, multi-observatory, and multi-spacecraft data that require more sophisticated display techniques in form of overlays, composite images, movies, animations, 3D reconstructions (e.g., Fig. 12), multi-media presentations, and web-based internet material. Also the publication process shifts more and more from printed journals to electronic files, even incorporating interactive 3D graphics in electronically published papers (Barnes and Fluke 2008). A mushrooming industry of software is currently developed that specializes on visualization of solar imagery. A (incomplete) list of some solar visualization software and URL links is provided in Table 5, which we summarize in the following.

The most popular software package used by solar physicists is *SolarSoft (SSW)* (Freeland and Handy 1998), which is a set of integrated software libraries, data bases, and system utilities (operating in the *Interactive Data Language (IDL)* software) that contain a number of image visualization tools, such as for cataloging, mapping, coalignment, overlays, and movie making. The *SSW*

Table 5. Software with visualization of solar imagery

Name	URL link
SolarSoftware (SSW)	http://www.lmsal.com/solarsoft/
SSW Latest Events	http://www.lmsal.com/solarsoft/latest_events/
Solarsites	http://www.lmsal.com/solarsites.html
SolarMonitor	http://www.solarmonitor.org/
Solar Weather Browser (SWB)	http://sidc.oma.be/SWB/
FESTIVAL	http://www.ias.u-psud.fr/stereo/festival/
iSolSearch	http://www.lmsal.com/helio-informatics/hpkb/
HelioViewer	http://www.helioviewer.org/
jHelioviewer	http://achilles.nascom.nasa.gov/˜ dmueller/
Aladin	http://aladin.u-strasbg.fr/

Latest Event website, maintained by Sam Freeland at Lockheed Martin Solar and Astrophysics Laboratory (LMSAL), displays a very useful synopsis of solar data in weekly time intervals, containing EUV, soft X-ray images, GOES light curves, ACE solar wind data, and magnetic field extrapolations. The *Solar-Monitor* website, hosted by the Solar Physics Group of Trinity College Dublin and NASA Goddard Space Flight Center's *Solar Data Analysis Center (SDAC)* displays near-realtime and archived information on active regions and solar activity, such as full-disk magnetograms, Hα, EUV, and soft X-ray images. The *Solar Weather Browser (SWB)* website, developed by the Royal Observatory of Belgium, is a software tool for easy visualisation and browsing of solar images (e.g., SOHO/EIT or GONG white light images) in combination with space weather data (i.e., NOAA active regions, plage locations, Catania sunspot groups, CACTUS CME detections), making use of web-distributed solar data and metadata (Nicula et al. 2008). *FESTIVAL* is an IDL-based browser designed for simultaneous display and fast manipulation of solar imaging data, including SECCHI/STEREO, EIT/SOHO, LASCO/SOHO, Nançay Radio Heliograph (NCR), Mauna Loa Mark-IV (MkIV), TRACE, and XRT/Hinode images (Auchere et al. 2008). The *iSolSearch* webpage, part of the *Heliophysics Events Knowledgebase (HEK)* hosted at LMSAL allows a user to interactively search for solar features and events using solar image data bases and event catalogs (e.g., AR locations, flares, CMEs). The *HelioViewer* website provides user-selected overlays of full-disk EUV images with solar features like LASCO CMEs, GOES X-ray flares, and NOAA active regions. The *jHelioviewer* offers an efficient visualization software of solar imagery using the *JPEG2000* image format (Müller et al. 2009). *Aladin* is a visualization tool of astronomical images and catalogues, providing a *Virtual Observatory (VO)* portal to the UK-based *AstroGrid* database, which includes also solar datasets (Dalla 2006). It is probably safe to say that each visualization software has its particular advantages and specialties, while none combines all data sets and capabilities, although the trend goes towards universal tools and complete interlinking of data bases.

Table 6. Major solar feature and event catalogs.

Name	URL link
Virtual Solar Observatory (VSO)	http://umbra.nascom.nasa.gov/vso/
	http://vso1.nascom.nasa.gov/docs/wiki/
Virtual Heliospheric Observatory (VHO)	http://vho.gsfc.nasa.gov/
Collaborative Sun-Earth Connector (CoSEC)	http://cosec.lmsal.com/
Heliophysics Event Knowledgebase (HEK)	http://lmsal.com/sungate/
European Grid of Solar Observations (EGSO)	http://www.egso.org/
Heliophysics Integrated Observatory (HELIO)	http://www.helio-vo.eu/index.php

5.2. Cataloguing of Solar Features

Metadata is defined as *"data about other data"* according to Wikipedia. Regarding solar databases, which contain zillions of images to-date, data analysis is only managable using feature and event catalogs that are organized by well-defined parameters and can be searched according to user-selected parameter combinations. The most frequently used solar catalogs contain lists of sunspot numbers, active regions, flares, CMEs, and radio bursts, but future catalogs based on *Solar Dynamics Observatory (SDO)* observations will also contain systematic records of nanoflares, coronal loops, quiescent filaments, eruptive filaments, prominences, oscillating loops, global waves, EUV dimmings, etc., which can only be gathered in an efficient way by automated feature detection algorithms, as described in Sections 3 and 4. New developments focus on content-based image retrieval (Csillaghy 1995, 1997, Csillaghy and Benz 1999; Csillaghy et al. 2000). The usability of solar feature catalogs will be enhanced by globally interlinked databases, world-wide access, web-browser capabilities, and sophisticated visualization tools. We list the major advanced solar feature catalogs in Table 6.

The *Virtual Solar Observatory (VSO)* is a distributed software that interconnects various solar databases and offers to the user a browser query interface with multiple search methods (or combinations) and a graphical user interface for sorting subsets of selected data (Gurman et al. 2005; Csillaghy et al. 2001). The SDO *Heliophysics Event Knowledgebase (HEK)* allows the user to query for "interesting" data subsets from SDO and commonly accessed datasets within the Joint Science Operations Center (JSOC) to optimize search and downloading time of desired data (Schrijver et al. 2008; Hurlburt et al. 2008, 2009). Subsets of this overarching metadata base have been previously accessed under the *Virtual Solar Observatory (VSO)*, the *Virtual Heliospheric Observatory (VHO)*, or the *Collaborative Sun-Earth Connecter (CoSEC)*. The *European Grid of Solar Observatory (EGSO)* is an earlier variant of a virtual solar observatory, funded by the European Community, which gives access to several dozens of solar databases, archives, feature, and event catalogs (Bentley et al. 2002, Zharkova et al. 2005a,b, Benkhalil et al. 2006, Aboudarham et al. 2006). HELIO, the successor of EGSO is scheduled to start in 2009.

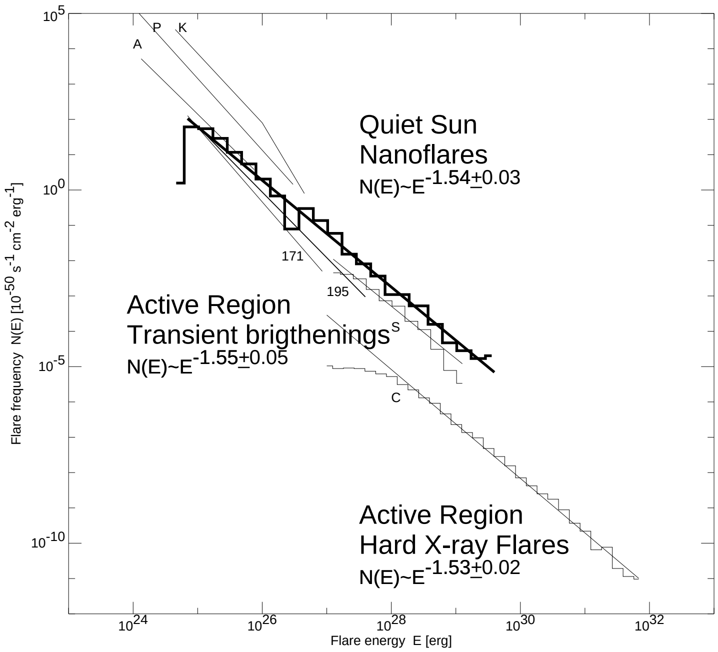

Figure 13. Compilation of frequency distributions of thermal energies from nanoflare statistics in the Quiet Sun, active region transient brightenings, and nonthermal energies from hard X-ray flares. The labels indicate the following studies: K=Krucker and Benz (1998), Benz and Krucker (2002), P=Parnell and Jupp (2000) [corrected for an erroneous factor of 100 in the original paper], A=Aschwanden et al. (2000b), S=Shimizu (1995), C=Crosby et al. (1993), [171,195]=Aschwanden and Parnell (2002). The overall slope of the synthesized nanoflare distribution, $N(E) \propto E^{-1.54 \pm 0.03}$, is similar to that of transient brightenings and hard X-ray flares. Note that the area of active regions is about two orders of magnitude smaller than that of the quiet Sun, which has to be taken into account when comparing the absolute occurrence rate. Also, the rate of active region phenomena is expected to vary about two orders of magnitude during the solar cycle, while the variation of quiet-Sun nanoflares during the solar cycle is not known [Aschwanden and Parnell 2002].

5.3. Statistics of Solar Events

How can we trust statistical distributions of observed parameters gathered by visual or manual measurements? Measurement errors may be evenly and randomly distributed if we plot distributions or histograms on a linear scale, but strong distorting biases are clearly introduced near the threshold of event statistics when distributions are plotted on a logarithmic scale. For instance, let us have a look at the frequency distribution of solar flare events shown in a log-log representation in Fig. 13, where statistics of the nonthermal flare energy contained in nonthermal electrons that emit hard X-rays at energies > 25 keV is accumulated for some 3000 flare events from SMM/HXRBS. We see a powerlaw distribution over the energy range of $E = 10^{28} - 10^{32}$ ergs, but clearly notice a turnover at the low energy range of $E = 10^{27} - 10^{28}$ erg. This turnover does not correspond to the true distribution, but is most likely caused by undersampling and truncation bias at the lower threshold value. If all flare events with energies of $E \geq 10^{27}$

erg could be sampled, no such turnover should occur. In this case, however, the observational statistics was gathered with a threshold in the hard X-ray peak count rate ($C > 100$ cts s^{-1}), rather than in energy, which causes a truncation bias because of the large scatter in the correlation between count rates and flare energies. This truncation bias is only part of the explanation for the turnover. Another source of error is the completeness of sampling near the threshold, which is very unreliable by visual recognition[1]. To avoid such systematic sampling biases based on human subjectivity that affect the mathematical function of the frequency distributions and the derived correlations and scaling laws between observed parameters, automated feature recognition is clearly desirable to obtain ultimate objectivity.

Frequency distributions, which quantify the occurrence rate of events as a function of a size parameter (e.g., peak count rate, total counts, total flux, fluence, thermal energy, nonthermal energy, event duration, etc.) became an important tool for theoretical modeling of nonlinear dissipative systems in terms of *self-organized criticality (SOC)* models. The powerlaw slope and deviations from it became crucial diagnostic tools to evaluate whether small events (e.g., nanoflares) or large events dominate the energy budget, which can be discriminated by the critical value of $\alpha = 2$ in the powerlaw slope (Hudson 1991). Most statistics of flare energies reveal a powerlaw slope of $\alpha \approx 1.5-1.6$ (Fig. 13). Flares associated with CMEs were found to have different powerlaw slopes than those without CMEs (Yashiro et al. 2006). For CMEs, the frequency distributions of kinetic energies was found to be $\alpha \approx 1.0$ (Vourlidas et al. 2002, 2009), so the correlation and corresponding scaling laws between flare and CME energies is not understood at this time. However, the flat slope of $\alpha \approx 1$ implies that the prevailing energy loss is in large CMEs, while the infitesimal sum of smaller CMEs can be neglected in the overall energy budget.

These are all examples of statistical studies that require automated feature recognition tools to detect events on all scales (usually spanning over several orders of magnitude) with equal reliability and objectivity. Although even automated detection schemes can have their own bias (e.g., selection criteria or instrument-dependent temperature sensitivity), they can be corrected using quantitative knowledge of the bias effect (e.g., using Monte-Carlo simulations to quantify selection criteria, or instrumental response functions to correct for temperature bias).

[1]There is a telling story in this case: Dr. Brian Dennis at NASA/GSFC supervised the generation of the SMM/HXRBS flare catalog over the entire time span of the mission during 1980-1990. Different data technicians were employed to visually identify and catalog all flares above a threshold of 100 cts s^{-1}. One particular technician, Bernie, some day got tired of recording the many tiny flare events during the solar maximum and started to ignore the tiniest events with count rates of $\lesssim 150$ cts s^{-1}, hoping nobody would notice. However, little did he know that log-log frequency distributions are very sensitive to such systematic truncations. Later, Dr. John Lawrence started to investigate the frequency distribution of HXRBS flares and noticed a significant deviation from a straight powerlaw at the lower end. It happened that he met Dr. Brian Dennis at an SPD meeting and shared with him a possible interpretation in terms of harmonic multi-fractals. Dr. Brian Dennis scratched his head, then started to laugh, and said “Oh no, this is the Bernie effect!”

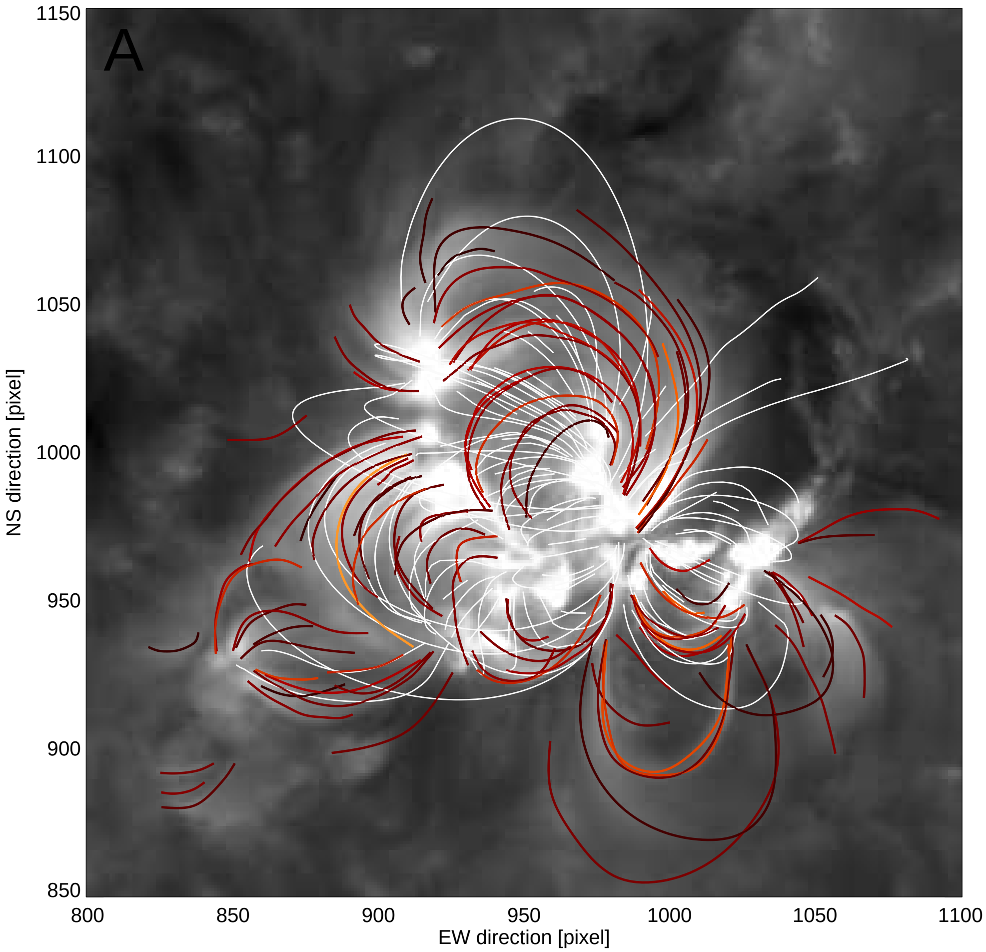

Figure 14. Example of a theoretically calculated potential magnetic field model (white), which is compared with observed EUVI loops triangulated with STEREO/EUVI (red color table) for AR 10956 on 2007 May 19. The background image is an EUVI image in 171 Å. The color indicates the average misaligment angle α between the potential field model and the real EUV loops: $\alpha \leq 30°$ (brown), $\alpha \approx 40°$ (red), $\alpha \approx 60°$ (orange), and $\alpha \geq 70°$ (yellow). [Sandman et al. 2009].

5.4. Theoretical Modeling

Many theoretical modeling efforts of solar physical processes require automated feature detection, because the models deal with measurements of features in space and time that need to be determined in large quantities and with high precision. We enumerate a few examples, because the type of physical modeling may influence the design of automated pattern recognition tools.

Some applications of 3D reconstruction modeling based on 2D feature detection in solar EUV images are: (1) theoretical modeling of the 3D coronal magnetic field in terms of potential or nonlinear force-free field extrapolations, constrained by the observed geometry of (automatically traced) EUV loops (Fig. 14), either in 3D with STEREO or in 2D projections with TRACE or SOHO/EIT (Aschwanden 2005; Feng et al. 2007; DeRosa et al. 2009; Sandman et al. 2009); (2) 3D reconstruction of active regions based on (automatically traced) EUV loops with stereoscopy-based tomography (Aschwanden et al. 2008a,b, 2009a), in contrast to standard (back-projection) tomography (Hurlburt et al. 1993; Frazin 2000; Frazin and Janzen 2002, Frazin and Kamalabadi 2005, Frazin et al. 2005) that does not require pattern recognition; (3) 3D reconstruction of (automatically traced) plumes with STEREO (Barbey et al. 2008, Feng et al. 2009, De Patoul et al. 2009); (4) 3D reconstruction of (automatically detected) CMEs contours from STEREO, using triangulation (de Koning et al. 2009), tomography (Frazin et al. 2009; Morgan et al. 2009), Kalman filters (Butala et al. 2005, 2006, 2008, 2009), polarimetric inversion (Moran and Davila 2004, Moran et al. 2006), forward modeling of flux rope models (Thernisien and Howard 2006, Thernisien et al. 2009); (5) 3D reconstruction of (automatically traced) prominences from STEREO using tomography (Vasquez et al. 2009, Thompson et al. 2009); or (6) 3D reconstruction of the kinematics of (automatically traced) CMEs in the inner heliosphere (Maloney et al. 2009).

5.5. Prediction and Forecasting

An indispensable (*sine qua non*) application of automated pattern recognition is real-time forecasting, because there is no time to detect and measure features in solar data sufficiently fast to deliver the forecast in near real-time (especially since spacecraft operators have nights, weekends and vacation too). The combination of automated pattern recognition and a parametric probabilistic prediction algorithm (enhanced with machine learning if possible), provides then a fully automated forecasting system. We mention a few initial studies in this direction.

Active region monitoring at the Big Bear Observatory, using Hα images from the Global Hα network, EUV, continuum, and magnetogram images from SOHO, and GONG data, provides near real-time predictions for each active regions to produce C-, M-, or X-class flares (Gallagher et al. 2002). Machine learning from sunspot classification, magnetogram data, solar cycle data, and CME catalogs can empirically find the best correlations between photospheric observables and coronal consequences in form of flares and CMEs, which can be used for automated short-term prediction of flares and CMEs (Qahwaji and Colak 2007, Qahwaji et al. 2008, Yuan et al. 2009, Qu et al. 2009; Yu et al. 2009). The automated detection and characterization of filaments (such as their chirality and geometry) allows us to monitor their evolution and possibly to predict their eruption, a major goal of space weather forecasting (Bernasconi et al. 2005). Furthermore, the automated tracking of CMEs (Robbrecht 2006, Olmedo et al. 2008) permits us to predict their trajectories and arrival time in geospace, which controls the local space weather.

6. Outlook and Future Trends

What will drive solar image processing techniques in the near future? The soon to be launched *Solar Dynamics Observatory (SDO)* (Pesnell 2008) is clearly on everybody's mind who works with solar data, because it will surpass all existing space-borne solar observatories in their capabilities. NASA's SDO fact sheet summarizes its capabilities succintly: *SDO will observe the sun, from its deep interior to the outermost layers of solar atmosphere, at the highest ever time cadence. SDO will snap a full disk image in 8 wavelengths every 10 seconds. This rapid cadence led to placing the satellite into an inclined geosynchronous orbit. This allows for a continuous, high-data-rate contact with a dedicated ground station at the White Sands Complex in southern New Mexico. SDO will send down about 1.5 terabytes of data per day, equivalent to downloading half a million songs each day. SDO's spatial resolution gives it a tremendous advantage over earlier missions. All solar images will be 4096 pixels $\times$ 4096 pixels - almost IMAX quality - providing details of the sun and its features that have rarely been seen before.* SDO has 3 instruments: the Helioseismic and Magnetic Image (HMI), the Atmospheric Imaging Assembly (AIA), and the Extreme Ultraviolet Variability Experiment (EVE).

On the other side, the solar physics community prepared in some way for this huge challenge by organizing a series of 4 *Solar Image Processing (SIP)* workshops over the last 8 years, which stimulated an exponentially increasing industry of new image analysis techniques, automated feature recognition codes, and involvement of artificial intelligence algorithms. Literature on solar image processing techniques has grown to over 200 refereed publications at the time of writing, with the majority been produced after the year 2000, which constitutes a faster growth rate than for the overall increase of $\approx$ 13 refereed solar publications per year (Fig. 2). We can therefore anticipate that efforts invested in the development, sophistication, and automation of new solar data analysis techniques will continue to grow at a fast pace during the next decade. New technologies also drive our handling and presentation of solar data. 3D DLP (chip) HDTV (high-definition television) sets are just becoming available for home entertainment, which can equally be used for display of 3D science data. The presentation of 3D reconstructions of solar active regions, filaments, flares, CMEs, and MHD simulations will benefit from such advanced off-the-shelf hardware, which doubtlessly will enter our future workshops and conferences. The availability of data analysis and numerical simulation codes will enable observers to interpret data with their own theoretical modeling and vice versa. Since many observables do not have a one-to-one correspondence with physical parameters, or are too complex to be modeled with physics-based models, algorithms with machine learning will be applied more widely, which will make trainable feature recognition modules more efficient. $-$ The sky is the limit!

Acknowledgements The author is grateful to many inspirations and discussions with colleagues, especially with participants of the four *Solar Imaging Processing (SIP)* workshops: Royal Observatory of Belgium, Brussels (SIP I: Oct 23-24, 2003), Annapolis (SIP II: Nov 3-5, 2004), Trinity College, Dublin (SIP III: Sept 6-8, 2006), and Baltimore (SIP IV: Oct

26-30, 2008), organized by Jack Ireland, Alex Young, and Peter Gallagher, with support from NASA's Living with a star program. The author is also grateful for the use of the *Astrophysical Database SYSTEM (ADS)*, operated by the Smithsonian Astrophysical Observatory (SAO) supported by NASA, which provided most of the information presented in this review. Part of the work was supported by the NASA TRACE (NAS5-38099) and NASA STEREO/SECCHI contracts (N00173-02-C-2035, administrated by NRL).

References

Aboudarham, J., Scholl, I., Csillaghy, A., Bentley, R.D., Antonucci, E., Ciminiera, L., Finkelstein, A., Ipson, S., Messerotti, M., Pike, D. 2006, Proc. International Heliophysical Year - First European General Assembly (ed. C. Briand), p.18.

Abramenko, V.I. 2005, *Solar Phys.* **228**, 29.

Adams, M., Hathaway, D.H., Stark, B.A., and Musielak, Z.E. 1997, *Solar Phys.* **174**, 341.

Aschwanden, M.J. 1995, *Lecture Notes in Physics* **444**, 13.

Aschwanden, M.J., Nightingale, R.W., Tarbell, T.D., and Wolfson, C.J. 2000a, *Astrophys. J.* **535**, 1027.

Aschwanden, M.J., Tarbell, T.D., Nightingale, R.W., Schrijver, C.J., Title, A.M., Kankelborg, C.C., Martens, P.C.H. and Warren, H.P. 2000b, *Astrophys. J.* **535**, 1047.

Aschwanden, M.J. and Parnell, C.E. 2002, *Astrophys. J.* **572**, 1048.

Aschwanden, M.J., Schmahl, E., and RHESSI Team 2002, *Solar Phys.* **210**, 193.

Aschwanden, M.J., Metcalf, T.R., Krucker, S., Sato, J., Conway, A., Hurford, G.J., and Schmahl, E. 2004, *Solar Phys.* **219**, 149.

Aschwanden, M.J. 2005, *Solar Phys.* **228**, 339.

Aschwanden, M.J., Lee, J.K., Gary, G.A., Smith, M., and Inhester, B. 2008a, *Solar Phys.* **248**, 359.

Aschwanden, M.J., Wuelser, J.P., Nitta, N.V., and Lemen, J.R. 2008b, *Astrophys. J.* **679**, 827.

Aschwanden, M.J., Nitta, N.V., Wuelser, J.P., and Lemen, J.R. Sandman, A. 2008c, *Astrophys. J.* **680**, 1477.

Aschwanden, M.J., Wuelser, J.P., Nitta, N.V., Lemen, J.R., and Sandman, A. 2009a, ApJ **695**, 12.

Aschwanden, M.J., Nitta, N.V., Wuelser, J.P., Lemen, J.R., Sandman, A., Vourlidas, A., and Colaninno, R.C. 2009b, *Astrophys. J.* (subm.).

Auchere, F., Subrie, E., Boccialini, K., and LeGall, F. 2008, *Solar Phys.* **248**, 213.

Balthasar, H. and Muglach, K. 2009, *Astron. Astrophys.* (in this volume).

Ballester, P. 1994, *Astron. Astrophys.* **286**, 1011.

Barbey, N., Auchere, F., Rodet, T., and Vial, J.-C. 2008, *Solar Phys.* **248**, 409.

Barnes, D.G. and Fluke, C.J. 2008, *New Astron.* **13/8**, 599.

Barra, V., Delouille, V. and Hochedez, J.F. 2008, *Adv. Space Res.* **42**, 917.

Barrow, J.D. 2008, *Cosmic Imagery. Key Images in the History of Science*, W.W. Norton & Company, New York, p.537.

Bastian, T.S. 2006, *Radio interferometry and Fourier synthesis imaging*, *http:// hesperia.gsfc.nasa.gov/summerschool/lectures/ bastian/Notes_on_Synth_Img.pdf.*

Benkhalil, A., Zharkova, V.V., Zharkov, S., and Ipson, S. 2006, *Solar Phys.* bf 235, 87.

Bentley, R.D. and EGSO Consortium 2002, in *Solar Variability: From Core to Outer Frontiers*, Proc. 10th European Solar Physics Meeting, ESA, ESTEC Noordwijk, Netherlands, (ed. Wilson, A.), Vol. **506**, 923.

Benz, A.O. and Krucker, S. 2002, *Astrophys. J.* **568**, 413.

Berger, T.E., Loefdahl, M.G., Shine, R.S. and Title, A.M. 1998, *Astrophys. J.* **495**, 973.

Bernasconi, P.N., Rust, D.M., and Hakim, D. 2005, *Solar Phys.* **228**, 97.

Bernasconi, P.N. and Georgoulis, M. 2009, *Solar Phys.* (in this volume).

Berrilli, F., Moro, D.D., Florio, A., and Santillo, L. 2005, *Solar Phys.* **228**, 81.

Bonet, J.A., Marquez, I., Muller, R., Sobotka, M., and Tritschler, A. 2004, *Astron. Astrophys.* **423**, 737.

Bovelet, B. and Wiehr, E. 2001, *Solar Phys.* **201**, 13.

Bovelet, B. and Wiehr, E. 2007, *Solar Phys.* **243**, 121.

Butala, M.D., Frazin, R.A., and Kamalabadi, F. 2005, *J. Geophys. Res.* **110**, 9.

Butala, M.D., Frazin, R.A., and Kamalabadi, F. 2006, AGU Fall Meeting, abstract #SH44-07.

Butala, M.D., Kamalabadi, F., Frazin, R.A., and Chen, Y. 2008, IEEE J. Sel. Topics Signal Proc., **2/5**, 755.

Butala, M.D. et al. 2009, *Solar Phys.* (in this volume).

Byrne, J.P., Gallagher, P.T., McAteer, R.T.J., and Young, C.A. 2009, *Astron. Astrophys.* **495**, 325.

Cadavid, A.C., Lawrence, J.K., and Ruzmaikin, A. 2008, *Solar Phys.* **248**, 247.

Chae, J. and Sakurai, T. 2008, *Astrophys. J.* **689**, 593.

Colak, T. and Qahwaji, R. 2008, *Solar Phys.* **248**, 277.

Collin, B. and Nesme-Ribes, E. 1995, *C. R. Acad. Sci. Ser. II*, Fasc. b, **321/2**, 77.

Conlon, P.A., Gallagher, P.T., McAteer, R.T.J., Ireland, J., Young, C.A., Kestener, P., Hewett, R.J., and Maguire, K. 2008, *Solar Phys.* **248**, 297.

Criscuoli, S., Moro, D.D., Bonet, J.A., and Marquez, I. 2005, *Solar Phys.* **228**, 177.

Criscuoli, S., Rast, M.P., Ermolli, I., and Centrone, M. 2007, *Astron. Astrophys.* **461**, 331.

Crockett, P., Jess, D.B., Mathioudakis, M., and Keenan, F.P. 2009, *MNRAS* (submitted).

Crosby, N.B., Aschwanden, M.J., and Dennis, B.R. 1993, *Solar Phys.* **143**, 275.

Csillaghy, A 1995, *Lecture Notes in Physics* **444**, 83.

Csillaghy, A. 1997, *Information extraction by local density analysis. A contribution to content-based management of scientific data*, (PhD Thesis), ETH Zurich, Shaker Verlag, Aachen.

Csillaghy, A. and Benz, A.O. 1999, *Solar Phys.* **188**, 203.

Csillaghy, A., Hinterberger, H., and Benz, A.O. 2000, *Information Retrieval* (Kluwer) Vol. **3**, 229.

Csillaghy, A., Zarro, D.M., and Freeland, S.L. 2001, *IEEE Signal Processing Magazine*, **18**, 41.

Csillaghy, A. 2009, *Solar Phys.* (in this volume)

Curto, J.J., Blanca, M., and Martinez, E. 2008, *Solar Phys.* **250**, 411

Dalla, S. 2006, *Solar system data access and analysis with AstroGrid*, *http://adass.org/adass2006/presentations/dallas.pdf.*

Davis, C., Bewsher, D., Davies, J., and Crothers, S. 2008, *Working with data from the NASA STEREO Heliospheric Imager an essential guide*, *http://www.sstd.rl.ac.uk/Stereo/Documents/ HI_user_guidejuly.pdf.*

DeForest, C.E. 2004, *Solar Phys.* **219**, 3.

DeForest, C.E. 2007, *Astrophys. J.* **661**, 532.

DeForest, C.E., Hagenaar, H.J., Lamb, D.A., Parnell, C.E. and Welsch, B.T. 2007, *Astrophys. J.* **666**, 576.

DeForest, C.E., Martens, P.C.H., and Wills-Davey, M.J. 2009, *Astrophys. J.* **690**, 1264.

De Koning, C.A., Pizzo, V.J. and Biesecker D.A. 2009, *Solar Phys.* **256**, 167.
Delouille, V., Patoul, J., Hochedez, J.F., Jacques, L. and Antoine, J.P. 2005, *Solar Phys.* **228**, 301.
Delouille, V., Chainais, P., and Hochedez, J.F. 2008, *Solar Phys.* **248**, 441.
DeMoortel, I. and McAteer, R.T.J. 2004, *Solar Phys.* **223**, 1.
Denker, C. 1998, *Solar Phys.* **180**, 81.
Denker, C., Yang, G., and Wang, H. 2001, *Solar Phys.* **202**, 63.
De Patoul, J., Feng, L., Inhester, B., and Wiegelmann, T. 2009, *Solar Phys.* (in this volume)
DeRosa, M.L., Schrijver, C.J., Barnes, G., Leka, K.D., Lites, B.W., Aschwanden, M.J., McTiernan, J.M., Regnier, S., Thalmann, J., Valori, G., et al. 2009, *Astrophys. J.* **696**, 1780.
De Wit, T.D. 2006, *Solar Phys.* **239**, 519.
De Wit, T.D., Moussaoui, S., Amblard, P.O., Aboudarham, J., Auchere, F., Kretzschmar, M., and Lilensten, J. 2009, in Proc. IEEE, Whispers conf. *Hyperspectral Imaging*, (in press).
Durak, N., Nasraoui, O., and Schmelz, J. 2009, *Pattern Recognition*, on-line, DOI: 10.1016/j.patcog.2009.03.10.
Durak, N. and Nasraoui, O. 2009, *Solar Phys.* (in this volume).
Feng, L., Inhester, B., Solanki, S.K., Wiegelmann, T., Podlipnik, B., Howard, R.A. and Wuelser, J.-P. 2007, *Astrophys. J.* **671**, L205.
Feng, L., Inhester, B., Solanki, S.K., Wilhelm, K., Wiegelmann, T., Podlipnik, B., Howard, R.A., Plunkett, S.P., Wuelser, J.P. and Gan, W.Q. 2009, *Astrophys. J.* (subm).
Fernandez Borda, R.A., Mininni, P.D., Mandrini, C.H., Gomez, D.O., Bauer, O.H., and Rovira, M.G. 2002, *Solar Phys.* **206**, 347.
Foullon, C. and Verwichte, E. 2006, *Solar Phys.* **234**, 135.
Frazin, R.A. 2000, *Astrophys. J.* **530**, 1026.
Frazin, R.A. and Janzen, P. 2002, *Astrophys. J.* **570**, 408.
Frazin, R.A. and Kamalabadi, F. 2005, *Solar Phys.* **228**, 219.
Frazin, R.A., Butala, M.D., Kemball, A., and Kamalabadi, F. 2005, *Astrophys. J.* **635**, L197.
Frazin, R.A., Jacob, M., Manchester, W.B.IV., Morgan, H., and Wakin, M.B. 2009, ApJ 695, 636.
Freeland, S.L. and Handy, B.N. 1998, *Solar Phys.* **182**, 497.
Fuller, N., Aboudarham, J., and Bentley, R.D. 2005, *Solar Phys.* **227**, 61.
Gallagher, P.T., Moon, Y.M., and Wang, H. 2002, *Solar Phys.* **209**, 171.
Gburek, S., Sylwester, J., and Martens, P.C.H. 2002, in *Multi-Wavelength Observations of Coronal Structures and Dynamics*, Proc. 10th Yohkoh Anniversary Meeting, (eds. Martens, P.C.H. and Cauffman, D.), COSPAR Coll. Ser., Elsevier, Amsterdam, Vol. **13**, 417.
Georgoulis, M.K. 2005, *Solar Phys.* **228**, 5.
Georgoulis, M.K., Raouafi, N.-E., and Henney, C.J. 2008, in *Subsurface and Atmospheric Influences on Solar Activity*, (eds. Howe, R., Komm, R.W.,, balasubramaniam, K.S., and Petrie, G.J.D.), ASP Conf. Series **383**, 107.
Georgoulis, M.K. 2009, *Solar Phys.* (in this volume).
Getling, A.V. and Buchnev, A.A. 2008, *Solar Phys.* **248**, 233.
Gissot, S. and Hochedez, J.F. 2007, *Astron. Astrophys.* **464**, 1107.
Gissot, S. and Hochedez, J.F. 2008, *Stat.Methodology* **5/4**, 340.
Gissot, S.F., Hochedez, J.F., Chainais, P., and Antoine, J.P. 2008, *Solar Phys.* **252**, 397.

Grec, C., Aime, C., Faurobert, M., Ricort, G., and Paletou, F. 2007, *Astron. Astrophys.* **463**, 1125.

Grosbol, R.H., Harten, R.H., Greisen, E.W., and Wells, D.C. 1988, *Astron. Astrophys. Suppl. Ser.* **73**, 359.

Gurman, J.B., Dimitoglou, G., Bogart, R.S., Tian, K.Q., Hill, F., Wampler, S., Martens, P.C., and Davey, A. 2002, American Geophysical Union, Fall Meeting 2002, abstract #SH52C-03.

Gurman, J.B., Dimitoglou,G., Hourcle, J., Bogart, R.S., Tian, K.Q., Hill, F/, Suarez-Sola, I., Wampler, S., Martens, P., Yoshimura, K., and Davey, A.R. 2005, *The Virtual Solar Observatory: Still in a Small Box*, *http://umbra.nascom.nasa.gov/vso/docs/AGU200505/Gurman_SH43B-03.pdf.*

Hagenaar, H.J., Schrijver, C.J. and Title, A.M. 1997, *Astrophys. J.* 481, 988.

Hagenaar, H.J., Schrijver, C.J., Title, A.M., and Shine, R.A. 1999, *Astrophys. J.* 511, 932.

Hagenaar, H.J., Schrijver, C.J. and Title, A.M. 2003, *Astrophys. J.* 584, 1107.

Hagenaar, H.J. and Shine, R.A. 2005, ApJ 635, 659.

Hamedivafa, H. 2008, *Solar Phys.* **250**, 17.

Harten, R.H., Grosbol, P., Greisen, E.W., and Wells, D.C. 1988, *Astron. Astrophys. Suppl. Ser.* **73**, 365.

Hewett, R.J., Gallagher, P.T., McAteer, R.T.J., Young, C.A., Ireland, J., Conlon, P.A., and Maguire, K. 2008, *Solar Phys.* **248**, 311.

Hudson, H.S. 1991, *Solar Phys.* **133**, 357.

Hurford, G.J. and Curtis, D.W. 2002, *Solar Phys.* **210**, 101.

Hurford, G.J., Schmahl, E.J., Schwartz, R.A., Conway, A.J., Aschwanden, M.J., Csillaghy, A., Dennis, B.R., Johns-Krull, C., Krucker, S., Lin, R.P., McTiernan, J., Metcalf, T.R., Sato, J., and Smith, D.M. 2002, *Solar Phys.* **210**, 61.

Hurlburt, N., Martens, P.C.H., Jaffey, S.M., and Slater, G.L. 1993, BAAS abstract #06.10, Vol. **25**, 1188.

Hurlburt, N., Cheung, M., and Bose, P. 2008, AGU Fall Meeting, abstract #SA53A-1580.

Hurlburt, N., Cheung, M., Schrijver, K., and the LMSAL HEK Team 2009, *Solar Phys.* (in this volume).

Inhester, B. 2006, *Stereoscopy basics for the STEREO mission*, eprint arXiv: astro-ph/0612649.

Inhester, B., Feng, L., and Wiegelmann, T. 2008, *Solar Phys.* **248**, 379.

Ipson, S., Zharkova, V.V., Zharkov, S., Benkhalil, A., Aboudarham, J., and Fuller, N. 2005, *Solar Phys.* **228**, 399.

Ipson, S., Zharkova, V., Zharkov, S., Benkhalil, A., Aboudarham, J., and Fuller, N. 2009, *AdSpR*, **43**, 282.

Ireland, J., Young, C.A., McAteer, R.T.J., WHelan, C., Hewett, R.J., and Gallagher, P.T. 2008, *Solar Phys.* **252**, 121.

Ireland, J., Marsh, M.S., Kucera, T.A., and Young, C.A. 2009, *Solar Phys.* in this volume.

Jess, D.B., Mathioudakis, M., Bloomfield, D.S., and Keenan, F.P. 2007, *Astron. Astrophys.* **473**, 943.

Jess, D.B., Mathioudakis, M., Erdelyi, R., Verth, G., McAteer, R.T.J., and Keenan, F.P. 2008, *Astrophys. J.* **680**, 1523.

Jones, H.P., Chapman, G.A., Harvey, K.L., Pap, J.M., Preminger, D.G., Turmon, M.J., and Walton, S.R. 2008, *Solar Phys.* **248**, 323.

Jones, H.P. et al. 2009, *Solar Phys.* (in this volume).

Karovska, M. and Hudson, H.S. 1994, in *New Look at the Sun with Emphasis on Advanced Observations of Coronal Dynamics and Flares*, (eds. S. Enome and

T. Hirayama), Nobeyama Radio Observatory Report, NOAJ, Nagano, Japan, No. **360**, 327.
Katsiyannis, A.C., Muglach, F., and Keenan, F.P. 2005, *Solar Phys.* **228**, 323.
Komm, R.W. 1994, in *Solar Active REgion Evolution: Comparing Models with Observations* (eds. Balasubramaniam, K.S. and G.W. Simon), ASP Conf. Ser. **68**, 24.
Komm, R.W. 1995, *Solar Phys.* **157**, 45.
Komm, R.W., Hurford, G.J., and Gary, D.E. 1995, *Astron. Astrophys. Suppl. Ser.* **122**, 181.
Krista, L.D. and Gallagher, P.T. 2009, *Solar Phys.* (in this volume).
Krucker, S. and Benz, A.O. 1998, *Astrophys. J.* **501**, L213.
LaBonte, B.J., Georgoulis, M.K., and Rust, D.M. 2007, *Astrophys. J.* **671**, 955.
Labrosse, N., Dalla, S., Marshall, S., and Gray, N. 2009, *Solar Phys.* (in this volume).
Lawrence, J.K., Cadavid, A., and Ruzmaikin, A. 2004, *Solar Phys.* **225**, 1.
Lee, J.K., Newmann, T.S., and Gary, G.A. 2004, in *Proc. 17th Internat. Conf. on Pattern Recognition*, Cambridge, UK, Aug 2004, p. IV315.
Lee, J.K., Newmann, T.S., and Gary, G.A. 2006a, *Pattern Recognition* (Elsevier), **39**, 246.
Lee, J.K., Newmann, T.S., and Gary, G.A. 2006b, in *Proc. 7th IEEE Southwest Symp. on Image Analysis and Interpretation*, Denver, March 2006, p.91.
Lefebvre, S. and Rozelot, J. 2004, *Solar Phys.* **219**, 25.
Lin, A.C., Nightingale, R.W., and Tarbell, T.D. 2001, *Solar Phys.* **198**, 385.
Liu, Y., Kurokawa, H., Kitai, R., Ueno, S., and Su,J.T. 2005, *Solar Phys.* **228**, 149.
Maloney, S.A., Gallagher, P.T., and McAteer, R.T.J. 2009, *Solar Phys.* (in this volume).
Marshall, S., Fletcher, L., and Hough, K. 2006, *Astron. Astrophys.* **457**, 729.
McAteer, R.T.J., Gallagher, P.T., Ireland, J., and Young, C.A. 2005, *Solar Phys.* **228**, 55.
McIntosh, P.S. 1990, *Solar Phys.* **125**, 251.
McIntosh, S.W. and Gurman, J.B. 2005, *Solar Phys.* **228**, 285.
McIntosh, S.W., DePontieu, B., and Tomczyk, S. 2008, *Solar Phys.* **252**, 321.
Metcalf, T.R., Hudson, H.S., Kosugi, T., Puetter, R.C., Pina, R.K. 1996a, *Astrophys. J.* **466**, 585.
Metcalf, T.R., Hudson, H.S., Kosugi, T., Puetter, R.C., Pina, R.K. 1996b, in Proc. *Maximum Entropy and Bayesian Methods*, (eds. K.M. Hansen and R.N. Silver), Kluwer, Dordrecht, Netherlands, p.361.
Mikurda, K. and Van der Luehe, O. 2006, *Solar Phys.* **235**, 31.
Mikurda, K., Tritschler, A. and Schmidt, W. 2006, *Astron. Astrophys.* bf 454, 359.
Moran, T.G. and Davila, J.M. 2004, *Science* **305**, 66.
Moran, T.G., Davila, J.M., Morrill, J.S., Dennis, W., and Howard, R. 2006, *Solar Phys.* 237, 211.
Morgan H. et al. 2009, *Solar Phys.* (this volume).
Mueller, D., Dimitoglou, G., Caplins, B., Ireland, J., Wamsler, B., Hughitt, K., Aghek-santerian, A., Amadigwe, E. and Fleck, B. 2009, *Comp. Science Eng.*, (subm).
Nakariakov, V.M. and King, D.B. 2007, *Solar Phys.* 241/2, 397.
Nicula, B., Berghmans, D. and Hochedez, J.-F. 2005, *Solar Phys.* **228**, 253.
Nicula, B., Marque, C., and Berghmans, D. 2008, *Solar Phys.* **248**, 225.
November,L.J., Toomre, J., Gebbie, K.B., and Simon, G.W., 1981, *Astron. Astrophys.* **245**, L123.
Ofman, L., Nakariakov, V.M., and Sych, R. 2009, *Solar Phys.* (in this volume).
Olmedo, O., Zhang,J., Wechsler, H., Poland, A., and Borne, K. 2008, *Solar Phys.* **248**, 485.

Olmedo, O., Zhang,J., Wechsler, H., Poland, A., and Borne, K. 2009, *Solar Phys.* (this volume).

Parnell, C.E. and Jupp, P.E. 2000, *Astrophys. J.* **529**. 554.

Perley, R.A., Schwab, F.R., and Bridle, A.H. 1980, *Synthesis Imaging in Radio Astronomy*, ASP Conf. Ser. Vol. **6**.

Pesnell, W.D. 2008, 37th COSPAR Scientific Assembly, Montreal, Canada, p. 2412.

Podladchikova, O.V. and Berghmans, D. 2005, *Solar Phys.* **228**, 265.

Portier-Fozzani, F., Vandame, B., Bijaoui, A., Maucherat, A.J., and EIT Team 2001, *Solar Phys.* **201**, 271.

Potts, H.E., Barrett, P.K., and Diver, D.A. 2003, *Solar Phys.* **217**, 69.

Potts, H.E., Barrett, P.K., and Diver, D.A. 2004, *Astron. Astrophys.* **424**, 253.

Potts, H.E. and Diver, D.A. 2008, *Solar Phys.* **248**, 263.

Preminger, D.G., Walton, S.R. and Chapman, G.A. 2001, *Solar Phys.* **202**, 53.

Press, W.H., Flannery, B.P., Teukolsky, S.A. and Vetterling, W.T. 1986, *Numerical Recipes. The Art of Scientific Computing*, Cambridge.

Puetter, R.C. 1995, in *Int J. Image Sys. & Techn.*, **6**, 314.

Puetter, R.C. 1996, in *Proc. SPIE*, **2827**, 12.

Puetter, R.C. 1997, in *Instrumentation for Large Telescopes*, (eds. J.M. Rodriguez Espinosa, A. Herrero, and F. Sanchez), Cambridge University Press New York, p.75.

Puetter, R.C. and Yahil, A. 1999, in *Astronomical Data Analysis Software and Systems VIII*, (eds. D.M. Mehringer, R.L. Plante, and D.A. Roberts), ASP COnf. Ser. **172**, 307.

Qahwaji, R. and Colak, T. 2007, *Solar Phys.* **241**, 195.

Qahwaji, R., Colak, T., Al-Omari, M., and Ipson, S. 2008, *Solar Phys.* **248**, 471.

Qu, M., Shih, F.Y., Jing, J., and Wang, H. 2003, *Solar Phys.* **217**, 157.

Qu, M., Shih, F.Y., Jing, J., and Wang, H. 2004, *Solar Phys.* **222**, 137.

Qu, M., Shih, F.Y., Jing, J., and Wang, H. 2005, *Solar Phys.* **228**, 119.

Qu, M., Shih, F.Y., Jing, J., and Wang, H. 2006, *Solar Phys.* **237**, 419.

Revathy, K., Lekshmi, S., and Nayar, S.R.P. 2005, *Solar Phys.* **228**, 43.

Rieutord, M., Roudier, T., Roques, S., and Ducottet, C. 2007, *Astron. Astrophys.* **471**, 687.

Robbrecht, E. and Berghmans, D. 2004, *Astron. Astrophys.* **425**, 1097.

Robbrecht, E. and Berghmans, D. 2005, *Solar Phys.* **228**, 239.

Robbrecht, E. 2006, Geophysical Monograph Series, *Solar Eruptions and Energetic Partices*, (eds. N. Gopalswamy, R. Mewaldt, J. Torsti), AGU Code GM1654300, , Vol. **165**, p. 33.

Robbrecht, E. 2007, PhD Thesis, Royal Observatory of Belgium.

Robbrecht, E., Berghmans, D., Van der Linden, R.A.M. 2009, *Astrophys. J.* **691**, 1222.

Rodriguez, L., Zhukov, A.N., Gissot, S., and Mierla, M. 2009, *Solar Phys.* **256**, 41.

Roumeliotis, G. 1995, *Astrophys. J.* **452**, 944.

Rosa, R.R., Karlicky, M., Veronese, T.B., Vijaykumar, N.L., Borgazzi, A.I., Sawant, H.S., Barbosa, E.B., Sych, R., and Mendes, O.jun. 2008, *Adv. Space Res.*, **42/5**, 844.

Sakurai, T. and Shin, J. 2001, *PASJ* **53**, 361.

Salakhutdinova, I.I. and Golovko, A.A. 2004, *Solar Phys.* **225**, 59.

Sandman, A., Aschwanden, M.J., Wuelser, J.P., DeRosa, M.L., and Alexander, D.: 2009, *Solar Phys.* , in press.

Scholl, I.F. and Habbal, S.R. 2008, *Solar Phys.* **248**, 425.

Schrijver, K., Hurlburt, N., Mark, C., Freeland, S., Green, S., Jaffey, A., Kobashi, A., Schiff, D., Seguin, R., Slater, G., Somani, A., and Timmons, R. 2008, AGU Fall Meeting 2008, abstract #SM11B-1619.

Sellah, S. and Nasraoui, O. 2008, in *Tools with Artificial Intelligence*, ICTAI'08, 20th IEEE Internat. Conf., Vol. **2**, 45.
Shih, F.Y. and Kowalski, A.J. 2003, *Solar Phys.* **218**, 99.
Shimizu, T. 1995, *PASJ* 47, 251.
Shine, R.A., Simon, G.W., and Hurlburt, N.E. 2000, *Solar Phys.* **193**, 313.
Simberova, S. and Flusser, J. 2005, *Solar Phys.* **228**, 165.
Simberova, S., Haindl, M., and Sroubek, F. 2009, *Solar Phys.* (in this volume).
Simon, G.W., Brandt, P.N., November, L.J., Scharmer, G.B., and Shine, R.A. 1994, *Solar Surface Magnetism* (eds. R.J. Rutten and C.J. Schrijver), Kluwer Academic Publishers, Dordrecht, p.261.
Smith, M. 2005, *http://www.mssl.ucl.ac.uk/twiki/bin/view/SDO/ LoopRecognition*.
Socas-Navarro, H. 2005a, *Astrophys. J.* **620**, 517.
Socas-Navarro, H. 2005b, *Astrophys. J.* **621**, 545.
Socker, D.G. 1998, *Proc. SPIE*, **3442**, 44.
Soummer, R., Ferrari, A., Aime, C., and Jillsaint, L. 2007, *Astrophys. J.* **669**, 642.
Sridharan, R., Venkatakrishnan, P., and Verma, V.K. 2002, *Solar Phys.* **211**, 395.
Sridharan, R., Dashora, N., and Venkatakrishnan, P. 2004, *Solar Phys.* **222**, 35.
Stark, B., Adams, M., Hathaway, D.H., and Hagyard, M.J. 1997, *Solar Phys.* **174**, 297.
Stenborg, G., and Cobelli, P.J. 2003, *Astron. Astrophys.* **398**, 1185.
Stenborg, G., Vourlidas, A., and Howard, R.A. 2008, *Astrophys. J.* 674, 1201.
Sych, R.A. and Nakariakov, V.M. 2008, *Solar Phys.* **248**, 395.
Sych, R.A., Nakariakov, V.M., Karlicky, M., and Anfinogentov, S. 2009a, *Astron. Astrophys.* (in press).
Sych, R.A., Anfinogentov, S., Ofman, L., and Nakariakov, V.M., 2009b, *Solar Phys.* (this volume)
Sylwester, J. and Sylwester, B. 1998, *Acta Astronomica* **48**, 519.
Sylwester, J. and Sylwester, B. 1999, *AcA* **49**, 189.
Sylwester, J. and Sylwester, B. 2004, *HvaOB* **28/1**, 71.
Terradas, J., Oliver, R., and Ballester, J.L. 2004, *Astrophys. J.* **614**, 435.
Thernisien, A.F. and Howard, R.A. 2006, *Astrophys. J.* **642**, 523.
Thernisien, A.F., Vourlidas, A., and Howard, R.A. 2009, *Solar Phys.* **256**, 111.
Thompson, W. 2006, *Astron. Astrophys.* **449**, 791.
Thompson, W., Kliem, B., and Toereok, T. 2009, *Solar Phys.* (in preparation).
Tkaczuk, R., Rieutord, M., Meunier, N., and Roudier, T. 2007, *Astron. Astrophys.* **471**, 695.
Turmon, M., Pap, J.M., and Mukhtar, S. 2002, *Astrophys. J.* **568**, 396.
Ulrich, R.K. 2001, *Astrophys. J.* **560**, 466.
Van Noort, M., Rouupe van der Voort, L., and Loefdahl, M.G. 2005, *Solar Phys.* **228**, 191.
Vasquez, A.M., Frazin, R.A., and Kamalabadi, F. 2009, *Solar Phys.* on-line DOI 10.1007/s11207-009-9321-1.
Vecchio, A., Carbone, B., Lepreti, F., Primavera, L., Sorriso-Valvo, L., Veltri, P., Alfonsi, G., and Straus, T. 2005a, *Phys. Rev. Lett.* **95**, 061102.
Vecchio, A., Primavera, L., Carbone, V., and Sorriso-Valvo, L. 2005b, *Solar Phys.* **229**, 359.
Vecchio,A., Carbone,V., Lepreti, E., Primavera,L., Sorriso-Valvo,L., Straus, T., and Veltri, P. 2008, *Solar Phys.* **251**, 163.
Veronig, A.M., Steinegger, M., Otruba, W., Hanslmeier, A., Messerotti, M., Temmer, M., Brunner, G., and Gonzi, S. 2000, in *The Solar Cycle and Terrestrial Climate*, (ed. A. Wilson), ESTEC, Noordwijk, Netherlands, **ESA SP-463**, 455.

Vourlidas, A., Buzasi, D., Howard, R.A. and Esfandiari, E. 2002, in *Solar Variability: From Core to Outer Frontiers*, Proc. 10th European Solar Physics Meeting, ESA, ESTEC Noordwijk, Netherlands, (ed. Wilson, A.), Vol. **506**, 91.

Vourlidas, A. and Howard, R.A. 2006, *Astrophys. J.* **642**, 1216.

Vourlidas, A. et al. (2009), (in preparation).

Watson, F., Fletcher, L., Dalla, S., and Marshall, S. 2009, *Solar Phys.* (in this volume).

Wells, D.C., Greisen, E.W., and Harten, R.H. 1981, *Astron. Astrophys. Suppl. Ser.* **44**, 363.

Wuelser, J.P. and 33 co-authors: 2004, *Proc. SPIE* **5171**, 111.

Yang, G., Denker, C., Xu, Y., and Wang, H. 2003, in *Current Theoretical Models and Future High Resolution Solar Observations: Preparing for ATST*, PASP Conf. Ser., San Francisco, California, Vol. **286**, 317.

Yashiro, S., Akiyama, S., Gopalswamy, N., and Howard, R.A. 2006, *Astrophys. J.* **650**, L143.

Young, C.A. and Gallagher, P.T. 2008, *Solar Phys.* **248**, 457.

Yuan, Y., Shih, F.Y., Ju, J., and Wang, H. 2008, AGU (subm.)

Yu,D., Huang, X., and Cui, Y. 2009, *Solar Phys.* **255**, 91.

Zharkov, S., Zharkova, V.V., and Ipson, S. 2005a, *Solar Phys.* **228**, 377.

Zharkov, S., Zharkova, V.V., Ipson, S., and Benkhalil, A. 2005b, *EURASIP J. Appl. Signal Proc.*, **15**, 2573.

Zharkov, S. and Zharkova, V.V. 2006, *Adv. Space Res.* **38**, 868.

Zharkov, S., Gavryuseva, E., and Zharkova, V. 2008, *Solar Phys.* **248**, 339.

Zharkova, V.V., Ipson, S.S., Zharkov, S.I., Benkhalil, A., Aboudarham, J., and Bentley, R.D. 2003, *Solar Phys.* **214**, 89.

Zharkova, V.V., Aboudarham, J., Zharkov, S., Ipson, S.S., Benkhalil, A.K., and Fuller, N. 2005a, *Solar Phys.* **228**, 361.

Zharkova, V.V., Aboudarham, J., Zharkov, S., Ipson, S.S., Benkhalil, A.K., and Fuller, N. 2005b, *Adv. Space Res.* **36**, 1604.

Zharkova, V.V. and Schetinin, V. 2005, *Solar Phys.* **228**, 137.

Zharkova, V.V. and Jain, L.C. (eds.) 2007, *Artificial intelligence in recognition and classification of astrophysical and medical images (Studies in computational intelligence)*, Springer: New York.

Zharkova, V. and Zharkov, S. 2008, *Adv. Space Res.* **41/6**, 881.